ABSTRACT

RODIO, JEFFREY J. Improved Modeling of Shock Layer Radiation for Venusian and Martian Atmospheres. (Under the direction of Dr. Hassan A. Hassan.)

Calculation of the radiative heat flux requires solving the radiative transfer equation which depends on the absorption and emission coefficients of the gas. These values are determined by the excitation and de-excitation of the various species under consideration. At present, heat transfer calculations for the Venusain atmosphere indicate discrepencies between theory and measurement. It is believed that this is a result of incorrect transition data for various transitions. The goal is to reconsider the contributions from the C_2 Swan ($d^3\Pi_g$ – $a^3\Pi_u$), CN Red ($B^2\Sigma$ – $X^2\Sigma^+$), CN Violet ($A^2\Pi_i$ – $X^2\Sigma^+$), and CO 4^+ ($A^1\Pi$ – $X^1\Sigma^+$) band systems.

Specifically, the Franck-Condon factors (FCF), r-centroids, and vibrational transition probabilities were calculated for each of the band systems and compared to the most current values available. The transitions between the lowest vibrational levels were found to be similar while the current values tended to be slightly larger for the transitions involving the upper vibrational levels.

Finally, the transition probabilities were incorporated into NEQAIR 2009 v5 and the results were compared to experiments done in NASA Ames' Electric Arc Shock Tube (EAST). The tests included a set of shock waves in a gaseous medium of CO_2/N_2 with velocities ranging from 7 to 12 km/s and pressures ranging from 0.5 to 2 Torr. The regions most affected by the new values were the vacuum ultra-violet and red regions producing mixed results. The shape of the intensities of the CO 4th positive band system was seen to improve but the intensities were below experiment and the C_2 Swan matched well causing better agreement in the red region. The blue and infra-red regions showed no appreciable change.

Improved Modeling of Shock Layer Radiation for Venusian and Martian Atmospheres

by
Jeffrey J. Rodio

A thesis submitted to the Graduate Faculty of
North Carolina State University
in partial fulfillment of the
requirements for the Degree of
Master of Science

Aerospace Engineering

Raleigh, North Carolina

2012

APPROVED BY:

Dr. Jack R. Edwards, Jr	Dr. Tarek Echekki

Dr. Hassan A. Hassan
Chair of Advisory Committee

BIOGRAPHY

The author was born in Durham, NC on July 29, 1986 to John and Denise Rodio. In 2005 he graduate from Walter Hines Page Highschool in Greensboro, NC and began enrollment at North Carolina State University where he majored in Aerospace Engineering. In the spring of 2009 the author graduated from N.C. State and in the fall of the same year, began graduate studies at the same university. He has been pursuing a Master's in Aerospace Engineering since.

ACKNOWLEDGEMENTS

The author would like to thank his advisor Dr. Hassan A. Hassan for his mentorship and patience during this project. He would also like to thank Dr. Dinesh Prabhu and Dr. Michael Barnhardt for their support and leadership while at Ames.

This work was supported in part by the National Space Grant College and Fellowship Program and NC Space Grant Consortium and by NASA Ames Research Center.

TABLE OF CONTENTS

LIST OF TABLES

LIST OF FIGURES

CHAPTER 1

Background

The current scientific community has a strong interest in all of the planets that make up our solar system for many reasons; not the least of which is the opportunity to learn more about how Earth may have evolved. These missions present many difficult and interesting design problems due to the many extremes in conditions that a craft making an interplanetary trip must face: the range of ambient temperature from 3 K (black body temperature of background radiation in Space) to >7000 K (entry into Venus' atmosphere at 9 km/s), the debri and particles moving through space at high speeds, the extended period of time the craft must travel before even taking a scientific reading, and the enormous distances that must be traversed with minimal control. These examples give an idea of the breadth of topics that must be considered for a successful mission to even our closest neighbors.

One such mission was the Pioneer Venus program, which was not only loaded with instruments to take measurements of Venus, but also carried instruments to provide validation of design parameters, such as recording the aerothermal environment during entry.

The Pioneer Venus program was the result of recommendations made by the Space Science Board of the National Academy of Sciences in the late 1960's and early 1970's[26]. The mission was comprised of two spacecrafts – an orbiter and a multiprobe. The multiprobe carried four individual probes, three small and one large, all of similar shape that were to eject from the multiprobe bus and enter Venus' atmosphere at different locations.

The Pioneer mission had many objectives though they mainly focused around collecting data about Venus' atmosphere from many perspectives. The multiprobe was tasked with determining the composition of the clouds, the composition and structure of the atmosphere from the surface

to a high altitude, and the general configuration of the atmosphere. While the orbiter also collected information on the atmosphere – mainly on the upper atmosphere and a planetary perspective on Venus's atmosphere and surface – it also was outfitted to get a detailed look at Venus' ionosphere, the interaction of the solar wind with the ionosphere and small magnetic fields in the vicinity, the planet's gravitational field harmonics, and gamma ray burst density for the solar system interferometer network.

The information provided by the Pioneer Venus probes on the entry conditions for vehicles entering at nearly the same velocities (11.54 km/s) but at different angles and of different sizes is invaluable to researchers and engineers tasked with designing similar probes. Each probe was outfitted with two thermocouples. One was located at or near the stagnation point and a second was located further back on the flank. These provided temperatures and allowed for accurate estimation of the heating rates throughout the entry event so that the heat shield performance could be gauged.

The heat shield accounted for 10% of the total mass of each of the Venusian probes[23], so it was within reason to over-estimate the necessary shielding for safety. However, the projections for the Galileo Jupiter missions put the heat shield mass as high as 40% of the total mass[23]. In such a case, any reductions in the required heat shielding would greatly reduce the overall mass and thus reduce the costs significantly and/or allow for more scientific equipment to be carried. The optimization of the design of craft for future missions to the various celestial bodies will depend strongly on our ability to accurately predict the contributions of radiation to the aerothermal environment of the craft.

W. C. Pitts and R. M. Wakefield presented the data from the thermocouples embedded in the heat shield of the Pioneer Venus probes along with some preliminary analysis over the time of the entry event[23]. This event was broken down into two phases of thermal conditions: the first phase encompassed primarily the heat pulse generated by the dynamic breaking and the second phase was comprised of the cooling of the heat shield to ambient atmospheric temperature. From these descriptions it is apparent that the ablation process takes place during the first phase.

Though the data was included, a full analysis of the first phase was not available at the time of publication of the report by Pitts and Wakefield[23]. However, the heat shield thickness after ablation could be estimated by combining the thermocouple readings of the second phase and known material properties. Based on the estimated amount of ablation, it was determined that the expected heat transfer rates were a conservative prediction.

These estimates, along with the temperature data of phase one, were used by researchers Chul Park and Hyo-Keun Ahn in an attempt to re-create the thermocouple data[22]. A previous attempt had been made by Park and Whitefield in 1980 to do this, but had resulted in unexpected results. As reported by Park and Ahn[22] about the previous work,

> ...the heat transfer rates seemed to have been overestimated for the stagnation region and underestimated for the frustum region.

The major differences between their work and previous works were a correction of the CO_2-N_2 mixture ratio for the Venusian atmosphere from $90-10\%$ to $97-3\%$, the use of a state-of-the-art line-by-line technique for the radiative heating, and the implementation of an updated pyrolysis model. The pyrolysis adjustment was, perhaps, the largest and most important adjustment because the pyrolysis-gases had a large effect on both the convective and radiative heating rates.

The final conclusion reached by Park and Ahn was that the flow was in nonequilibrium in the boundary layer which brought the convective heat transfer rates down by 1/3 of the values determined by assuming equilibrium and that a significant amount of radiation was absorbed by the pyrolysis-gases.

As was explained by Pitts and Whitefield in 1980, the higher velocity entries associated with missions to bodies farther away than Earth's Moon inevitably increases the importance of radiative heating on the entry vehicle. The heating rates for missions to Venus have a nearly equivalent input from convective and radiative sources, but the heating rates for missions to Jupiter are overwhelmingly due to radiation[23]. The effects of the pyrolysis-gases explain some of this. As the gas injection rate increases, the boundary layer is pushed farther from the surface. At high enough rates, the boundary layer is blown completely off, reducing the amount of convective heating significantly[23].

Park and Ahn noted that the radiation affected the temperature distributions significantly. To summarize some of their findings, the radiation partially cools the hot inviscid region and heats up the cooler boundary layer. The pyrolysis-gases absorbed a large amount of the radiation which served to increase the effective convective heating rates.

CHAPTER 2

Introduction

There are three main flow regimes that a vehicle passes through during entry into a planet's atmosphere. These are free molecular, transitional, and continuum flow; distingushable by the mean free path of the molecules in each. Free molecular flow generally has a Knudsen number ($K_n = \frac{\lambda}{D}$ where λ is the mean free path and D is some characteristic length) of 10 or greater and is characterized by rare collisions between molecules, meaning the internal modes tend to stay "frozen" at initial conditions. Continuum flow, $K_n < 0.1$, has many collisions between molecules. In this regime equilibrium flow becomes possible as the local collisions outweigh the collision history of the independent molecules [8]. Transitional flow does as the name implies and bridges the gap between free molecular and continuum flow, a frozen flow is possible in the upper limits while non-equilibrium begins as the molecular collisions increase. The continuum regime is where the majority of the heating takes place do to its high level of molecular interactions and molecule-vehicle interactions.

A vehicle enters the atmosphere at hypersonic speeds (Mach numbers of 20 or greater) producing a strong bow shock which serves to heat, dissociate, and ionize the gas as the vehicle passes. A strong shock can excite the electronic states of molecules which then give off energy in the form of radiation. For sufficiently high velocities radiation begins to play an important role in the aerothermal environment. The radiation can transport energy from the hot main flow to the cooler boundary layer and to the surface of the vehicle itself. This affects both the aerodynamic coefficients (lift, drag, etc.)[8] as well as the heating rates of the vehicle. From an engineering stand point, the task then becomes how to include the affects of radiation in the governing equations.

There are three terms to consider with the inclusion of radiation; the radiant energy, radiation pressure, and radiative heating. The radiant energy density scales with temperature to the fourth, T^4, while the thermal energy scales with the number density times the temperature, nT. Ultimately what can be shown [29] is that the temperature at which the radiation energy and the thermal energy become equal scales with the cube root of the number density, $n^{1/3}$. The radiation pressure and fluid pressure share a similar relationship. In continuum flow where the number densities are large, the radiant energy and radiation pressure do not have an effect on the motion or energy of the flow. The third term, the radiative heating can become very important and must be considered in a hypersonic shock heated flow.

The radiant heat flux vector can be expressed as[28]:

$$q_i^R = \int_0^\infty \int_0^{4\pi} I_\lambda l_i d\Omega d\lambda \tag{2.1}$$

where I_λ is the spectral intensity at wavelength λ and l_i is the direction cosine for direction i. Ω is the solid angle which spans 4π steradians.

The evaluation of the spectral intensity requires solving the radiative transport equation

$$\frac{1}{c}\frac{\partial I_\lambda}{\partial t} + l_i \frac{\partial I_\lambda}{\partial x_i} = \epsilon_\lambda - k_\lambda I_\lambda \tag{2.2}$$

where ϵ_λ is the emission coefficeint, k_λ is the absorption coefficient, and c is the speed of light in a vacuum. Given the magnitude of c, the time dependent term is generally dropped.

An analogous way to write the radative transfer equation is to replace the vector expression with a directional derivative. This is the form that will be used in the following analysis as it provides an easy way to visualize the affects of the equation without loss of generality. Let s lie along the solid angle that describes the direction of propogation, then the steady state equation becomes:

$$\frac{dI_\lambda}{ds} = \epsilon_\lambda - k_\lambda I_\lambda \tag{2.3}$$

The emission and absorption coefficients are calculated using a line-by-line method. This means that they are determined using the transition information for all of the transitions being considered. The transitions are dependent on the molecular make-up of the gas and thus the contributions may change as the gas composition changes.

There are presently a number of programs written for solving the radiative trasnfer equation. This work focuses on the code used by NASA Ames Research Center called NEQAIR 2009 v5 [21]. NEQAIR is a spectral high-resolution line-by-line code for computing intensities of atomic lines/continua and diatomic molecular band systems and transporting these intensities from the shock front to the body along a line of sight by first-order integration of the radiative transport equation. The code is currently being used for estimating radiative heating of several Venus

probes.

NEQAIR is calibrated against experiments conducted in the Ames Electric Arc Shock Tube (EAST) facility. Although no direct measurements are made of radiative heating, the shock tube provides a way of heating a representative gas mixture (N_2/O_2, CO_2/N_2, H_2/He) with a shock traveling at velocities representative of flight. Sophisticated instrumentation, such as spectrometers, photo-multiplier tubes, etc, are used to record the optical signal from the shock-heated gas.

The EAST facility's four spectrometers, each at the same axial location but different azimuthal angles, are capable of capturing spectral and spatial resolution for radiation ranging from 110 nm to 1.65 μm. As of 2010, it was the only facility collecting radiation measurements from the vacuum ultraviolet region, a large contributor to the radiative heating under the conditions of a Venus entry[3].

Experiments capture the time relaxation of the shock-heated flow from behind the traveling shock to some distance downstream, and NEQAIR is used in simulation of spectral radiance in the region between the shock wave and slip line. This region is often assumed to be in thermal and chemical equilibrium; however, time-accurate calculations of the flow in the EAST facility that allow for thermal and chemical non-equilibrium show otherwise [15, 16]. Comparison of spectral features and intensities against measurements provides a first calibration of NEQAIR and confidence in the predicted levels of radiative heating for an entry probe.

Presently of interest are a set of experiments conducted in the EAST facility for CO_2/N_2 gas mixtures (representative of Mars or Venus atmosphere). Some of the major findings from a previous round of NEQAIR simulations were:

- A key feature of the C_2 Swan band ($d^3\Pi_g$ - $a^3\Pi_u$) was shifted to smaller wavelengths than expected from theory. As a consequence, the integrated intensity over the 500-520 nm wavelength range (in the Red region) was well below the experimental value.

- The wavelength integrated intensity in the vacuum-ultra violet (VUV or wavelengths less than 200 nm) was in close agreement with the value computed from the measured spectrum; however, the actual distributions of the intensities due to the CO 4th positive ($A^1\Pi$ - $X^1\Sigma^+$) band system were seen to be significantly different from measurements.

- In the blue (wavelength range from 190 nm to 490 nm) the integrated intensity is under predicted.

- In the infra-red (wavelength range from 1050 nm to 1650 nm) regions, the integrated intensities for the predictions and experiments showed good agreement; however, there are exaggerated features and lower than measured background continuum radiation.

The goal of this work is to enhance the agreement between NEQAIR 2009 v5 and the data from EAST by updating the diatomic band system information. This requires the calculation of the vibrational transition moments of four band systems; so chosen because of their influence in the problematic regions. The electronic band systems chosen for the present work are:

- The C_2 Swan band ($d^3\Pi_g$ – $a^3\Pi_u$).
- The CO 4th positive band ($A^1\Pi$ – $X^1\Sigma^+$).
- The CN Violet band ($B^2\Sigma$ – $X^2\Sigma^+$).
- The CN Red band ($A^2\Pi_i$ – $X^2\Sigma^+$).

This should improve the accuracy of NEQAIR and thereby allow for a better prediction of radiative heating rates during entry into CO_2/N_2 containing atmospheres such as Venus and Mars.

CHAPTER 3

Radiative Heating Estimation

The effects of radiation emission and absorption on both the flow field and heat transfer rates become significant for high temperature flows such as entry events. The attempts to model the heating rates have proven to be difficult and have shown a need to further refine the tools being used.

As was mentioned in the introduction, the effects of radiation are included in the governing equations by the radiative heating term in the energy equation.

The conservation equations of mass and momentum are the same as for any compressible hypersonic flow. Omitting body forces these equations can be written as:

$$\frac{\partial \rho_i}{\partial t} + \frac{\partial(\rho_i(u_j + w_j))}{\partial x_j} = R_i \tag{3.1}$$

$$\frac{\partial(\rho u_i)}{\partial t} + \frac{\partial(\rho u_i u_j)}{\partial x_j} = -\frac{\partial P}{\partial x_i} + \frac{\partial(\tau_{ij})}{\partial x_j} \tag{3.2}$$

where ρ is the total density, ρ_i is the density of species i, R_i is the production rate of species i, u_i is the velocity, w_i is the diffusion velocity, P is the pressure, and τ_{ij} is the shear stress.

The energy equation simply requires an additional heat transfer term, i.e. the loss of heat due to radiation.

$$\frac{\partial E}{\partial t} + \frac{\partial(E u_j)}{\partial x_j} = -\frac{\partial(P u_j)}{\partial x_j} + \frac{\partial(u_i \tau_{ij})}{\partial x_j} - \frac{\partial q_j^R}{\partial x_j} - \frac{\partial q_j}{\partial x_j} \tag{3.3}$$

where E is the total energy ($\rho(e_{internal} + \frac{1}{2}u_i u_j)$), q_j^R is the radiant heat flux vector, and q_j is

heat flux vector for sources other than radiation.

The radiative heating term in the energy equation can be evaluated once we know exactly what it is. The radiant heat flux is composed of the total radiance propogating in a particular direction. For example, in cartesian standard basis this would be in one of the x, y, or z directions (x_1, x_2, x_3, respectively, in tensor notation). By total radiance we mean all of the contributions from each wavelength together from all directions. This equation was introduced early (2.1)

$$q_i^R = \int_0^\infty \int_0^{4\pi} I_\lambda l_i d\Omega d\lambda \tag{3.4}$$

where, again, I_λ is the spectral intensity at wavelength λ and l_i is the direction cosine for direction i. Ω is the solid angle which spans 4π steradians.

To evaluate I_λ the radiative transfer equation (RTE) must be solved. This equation propagates the radiance from an inital point or points through a medium to a final destination. This allows for the spectral intensities of each wavelength to be known at a given location in the medium.

3.1 Radiative Transfer Equation

This deceptively simple equation can be generally written as [11]:

$$\frac{dI_\lambda}{ds} = \epsilon_\lambda - k_\lambda I_\lambda \tag{3.5}$$

where I_λ is the spectral intensity of wavelength λ, s is the optical path, ϵ_λ is the emission coefficient, and k_λ is the absorption coefficient. The solution of 3.5 is

$$I_\lambda(s) = I_\lambda(0)e^{-\tau_\lambda} + \int_0^{\tau_\lambda} e^{-(\tau_\lambda - \tau'_\lambda)} S_\lambda(\tau'_\lambda) d\tau'_\lambda \tag{3.6}$$

where $I_\lambda(0)$ is the incident radiation, $\tau_\lambda \equiv \int_{s_0}^{s} k_\lambda ds'$, and $S_\lambda \equiv \epsilon_\lambda / k_\lambda$. S_λ is a source function which may be taken to be the Black Body spectrum given by the Planck function, B_λ (Eqn. 3.7), if local thermodynamic equilibrium may be assumed. Because thermodynamic equilibrium is established very quickly [29], it is normally assumed that the flow is in local thermodynamic equilibrium.

$$B_\lambda = \frac{2hc^2}{\lambda^5} \frac{1}{e^{hc/(\lambda k_b T)} - 1} \tag{3.7}$$

where k_b in the above is the Boltzmann constant, h is the Planck constant, and c is the speed of light.

For a homogeneous medium Eq. 3.6 becomes[11, 21]

$$I_\lambda = I_\lambda(0)e^{-\tau_\lambda} + B_\lambda(1 - e^{-\tau_\lambda}) \tag{3.8}$$

The necessary components to solve Eq 3.8 are the incident radiation $I_\lambda(0)$, the temperature along the optical path T (required to determine B_λ), and the absorption coefficient k_λ (required to calculate τ_λ).

The homogeneous solution can be used to calculate the radiative transport across a non-homogeneous gas if the domain can be discretized into elements which are then approximated as homogeneous. Equation 3.8 can then be applied to each element in turn. In this case, there is a temperature for each element of gas and the incident radiation refers to the radiation at the beginning of the element (local coordinate $s = 0$). This is the scheme that NEQAIR uses to solve the RTE.

The absorption coefficient can be found through the source function, S_λ, which relates it to the emission coefficient, ϵ_λ. The emission coefficient can be evaluated by multiplying a line shape function by the spontaneous emission intensity whose expression was developed by Einstein[20].

$$\epsilon_\lambda = \epsilon\phi_\lambda \tag{3.9}$$

$$\epsilon = \frac{g_u N_u A_{ul} hc\bar{\nu}_{ul}}{4\pi} \tag{3.10}$$

where ϕ is a line shape function (a Voigt line shape is generally used), g_u is the degeneracy of the upper state, N_u is the number density of the upper state, $\bar{\nu}_{ul}$ is the energy differences between the upper and lower states, A_{ul} is Einstein's transition probability for spontaneous emission, and h and c are as before. Here, the spontaneous emission intensity, Eq. 3.10, was divided by 4π so as to provide the intensity in a single direction.

The number density of the excited state can be determined in a number of ways[11, 21], the major factor being whether to assume an equilibrium distribution or not. In this case, an equilibrium distribution is used. The degeneracies, energy differences, and Einstein coefficients are handled by current theory and can be experimentally verified.

3.2 Einstein Coefficients

The energies of each state and thus the degeneracies can be both computed and determined by experiment through a number of means. The most often used method is the Dunham expansion, which uses a few molecular constants and is more formally explained in reference [5].

The Einstein coefficients require yet further computation, the expression for which can be found in many places, such as Seong-Yoon Hyun's Doctoral thesis[11], M. Larsson's *Conversion*

formulas between dynamic variables in diatomic molecules[14], and P̆hysics of Shock Waves and High-Temperature Hydrodynamic Phenomena by Zel'dovich and Raizer[29], to name a few. The coefficient is expressed as

$$A_{v'J',v''J''} = \frac{64\pi^4 e^2 a_0^2}{3h} \bar{\nu}^3_{v'J',v''J''} \frac{\mathcal{S}_{J',J''}}{(2J'+1)} \tag{3.11}$$

where a_o is the Bohr radius, J' is the rotational quantum number, and $\mathcal{S}_{J',J''}$ is the line strength. The line strength is evaluated formally by taking the square of the integration of the product of the wavefunctions that describe the upper and lower states of the transition and the total transition operator over the internuclear distance and summing these values[14] (Equation 3.12).

$$\mathcal{S}_{J',J''} = \sum_{M',M''} | < \psi_{M'} | \bar{\mu} | \psi_{M''} > |^2 \tag{3.12}$$

where $\bar{\mu}$ is the total transition operature and ψ are the wavefunctions describing the upper and lower magnetic states.

The Born-Oppenheimer approximation says that since the speeds of the electrons are much greater than those of the nuclei, the motion of the nuclei has little affect on the electronic transition and therefore each wavefunction can be represented as the product of two (or more) wavefunctions[7] ($\psi_M = \psi_{elect}\psi_{nuc}$). This approximation allows the terms inside of the integral in Eq. 3.12 to be separated into a part that is governed by the electronic coordinates and one that is governed by the nuclear coordinates.

The contribution of the electrons becomes very difficult to solve analytically as the number of electrons increases. The orbitals become much more complex and though there are theories and methods used to solve for these functions, it is currently more applicable to use experimentally determined values. Thus, the electronic contribution is expressed as a curve that defines the eletronic transition moment with respect to the internuclear distance. Generally this equation is of the order of a cubic equation at most.

Further, the Condon approximation assumes that the electronic transition moment remains constant[7], which is perhaps not rigorously true; but it allows the removal of the electronic transition moment from inside of the integral in the line strength equation (Eqn. 3.12). Through the years, the experimental data seems to be showing more conclusively that this is not a very good approximation for all band systems [12, 18]. Obviously the exact system under consideration may have a near constant electronic transition moment, but others show a more varied response. The early functions were constant, then linear, and currently tend to be fit well by a quadratic equation.

If the condon approximation is made, the line strength equation becomes:

$$\mathcal{S}_{J',J''} = q_{v'J',v''J''} R_e^2(\bar{r}_{v'J',v''J''}) \mathcal{L}_{J',J''} \tag{3.13}$$

where $q_{v'J',v''J''}$ is the Franck-Condon factor (FCF, Eq. 3.14), $R_e^2(\bar{r}_{v'J',v''J''})$ is the electronic transition moment function (ETMF) evaluated at the r-centroid of the transition (Eq. 3.15), and $\mathcal{L}_{J',J''}$ is the Hönl-London factor. The r-centroid refers to the internuclear distance for which the transition is most likely to occur and the Frank-Condon factor is the square of the overlap integral. The Hönl-London factors reflect how the spin angular momentum and the orbital angular momentum pair up and thus the formulation depends on which Hund's cases the transition involves.

$$q_{v'J',v''J''} = \langle \psi_{v'J'} | \psi_{v''J''} \rangle^2 \tag{3.14}$$

$$\bar{r}_{v'J',v''J''} = \frac{\langle \psi_{v'J'} | r | \psi_{v''J''} \rangle}{\langle \psi_{v'J'} | \psi_{v''J''} \rangle} \tag{3.15}$$

3.3 Vibrational Transition Moments

The combination of the Franck-Condon Factor and the electronic transition moment function is known as the transition moment because it estimates the likelihood that the particular jump will occur. In NEQAIR, the rotational lines are not accounted for, leaving only the vibrational bands. Thus the line strength is actually composed of the vibrational transition probability (Eq. 3.17) multiplied by the Hönl-London factor. Equations 3.13, 3.14, and 3.15 are the same except for the dropping of the rotational quantum number from the Franck-Condon factor ($q_{v',v''}$) and the r-centroid ($\bar{r}_{v',v''}$).

$$S_{J',J''} = p_{v',v''} \mathcal{L}_{J',J''} \tag{3.16}$$

$$p_{v',v''} = q_{v',v''} R_e^2(\bar{r}_{v',v''}) \tag{3.17}$$

The notation makes this seem a trivial adjustment, but quantitatively this means that the wavefunctions come from solving the non-rotating time-independent Schrödinger's equation which is marginally simpler, and significantly reduces the number of calculations required.

The omission of the rotational part means that the fine rotational structure may be inaccurate in what is finally calculated, but the vibrational structure is sufficient for these types of calculations. The band head and vibrational structure provide a reasonably high resolution spectrum that is generally finer than is necessary for heating rate estimations.

One of the pieces of information that NEQAIR requires to solve the RTE is the square root of the vibrational transition moment ($\sqrt{p_{v',v''}}$) for each vibrational transition of each band system being considered. These transition moments are what are being recalculated using *ab initio* methods to provide more current values and hopefully increase the agreement between the calculated spectra and the experimentally determined one.

3.4 The r-Centroid Approximation

As it has already been mentioned, it is known that the electronic transition moment depends on the distance between the nuclei and that the approximation of a constant for the entire line strength integral is not fully correct. However, due to a couple of factors, it is still the norm for a line strength calculation to retain this assumption.

First, the functions are difficult to determine and the range over which they are applicable tends to be less than actual domain of the wavefunctions. This poses a problem when the integral is being evaluated. The functions could be extrapolated depending on how much of the domain is missing but as mentioned before, the way in which it varies may not be well represented by the current data. Of course, practically, these functions only need to be specified over the range for which the product of the wavefunctions is not zero. On an individual basis, this range tends to be smaller than the wavefunctions themselves; but unfortunately, the higher vibrational levels have correspondingly large ranges and thus the electronic transition moment function must still span a significant internuclear distance if one wants to include these transitions. An approximation simply must be made for the cases where the function does not span the range.

Second, the lower vibrational levels are the most abundantly populated – especially when assuming a Boltzmann distribution – and these levels have narrower overlaps. Thus the range of internuclear distances which need be considered is smaller. Even for a function with a large slope across this range, if the range is small enough, it may not introduce an exhorbitant amount of error by assuming a single value to represent the range.

The final consideration is that the product functions themselves have dominant features which are surrounded by near zero values. The electronic transition moment may vary largely; but if the product functions have large regions of near zero values, the effects of the variations will be mitigated. The r-centroid of the product functions is intended to determine a value to represent the range where the largest contributions come from and thus provide a fairly accurate approximation of the electronic transition moment for use with the overall integral.

Further, it has been shown by Noda and Zare[19] that the quantum mechanical formulation, i.e. r-centroid approximation, tends to correspond to the classical transition points. The Franck principle states that when an electronic transition takes place in a molecule, the positions and momenta of the nuclei tend strongly to remain constant. This leads to the quantum mechanical

formulation known as the Franck-Condon principle[17], which states that the most probable transitions are those that conserve position and kinetic energy in a classical sense. For transitions where there is one classical transition, the r-centroid tends to fall on this point. They also show how a transition which has more than classical transition point can be utterly misrepresented by assuming a single value. The r-centroid can lie quite far away from any of the transition points. Their solution (the Generalized r-Centroid Approximation) was to incorporate r-centroids of pieces of the wavefunctions chosen such that they match the classical transition points. Their method requires the knowledge of one or more of the classical transition points and then the necessary bounds can be determined to find the missing one.

Needless to say, this is difficult to incorporate into a generalized frame work as you would need the experimental data of most of the transition points anyways, and have to solve for the classical transitions simply to show there are multiple transition points to consider. As Noda and Zare note, the validity of the approximation can be guaged by considering the variance of the r-centroid. i.e.

$$(\Delta\bar{r})^2 = \bar{r^2} - \bar{r}^2 \tag{3.18}$$

Equation 3.18 allows one to pick out transitions that are most likely to be poorly approximated by using the r-centroid. The caveat being that though it is known that the variance should be close to zero, how close is close enough is not provided. This leaves some ambiguity when using this metric.

3.5 Wavefunctions

The wavefunctions that are necessary for calculating the FCF's and the r-centroids are determined by solving the non-rotating time-independent Schrödinger's equation. This was done using QUANTUM[24], a program written by Dr. Dinesh Prabhu. It uses a finite element method (the Discontinuous Galerkin's method) to solve for the energies and wavefunctions for each of the vibrational modes of a diatomic molecule.

$$\left(-\frac{\hbar^2}{2\mu}\nabla^2 + V(r)\right)\psi(r) = E\psi(r) \tag{3.19}$$

where $V(r)$ is the potential function (a combination of the electronic energy and the nuclear repulsion), μ is the reduced mass, ∇^2 is the kinetic energy operator, $\hbar$ is the Planck constant divided by 2π, E is the energy of the vibrational level, and $\psi(r)$ is the wavefunction.

A potential function must be assumed to solve Eq. 3.19. QUANTUM provides multiple potentials ranging from a harmonic oscillator to the Hulburt-Hirschfelder (5 paramter) potential. The Hulburt-Hirschfelder potential was used for each of the electronic states of all of the diatomic

molecules of interest. The evaluation of the chosen potential requires 5 parameters to be supplied: the dissociation energy De (not to be confused with the molecular constant D_e), the equilibrium bond length r_e, the term energy T_e, the blank ω_e, and the blank $\omega_e x_e$. The values used for each molecule are listed in Appendix A.

CHAPTER 4

NEQAIR

NEQAIR requires a number of inputs to run. Along with the species' spectroscopic constants, the flow conditions at a series of points throughout the domain must be defined. The flow conditions are generally taken from CFD solutions or measurements taken during experiment. The present conditions were chosen to match the conditions of the EAST experiments, in composition, concentration, and temperature.

The program Chemical Equalibrium with Applications (CEA)[9] was used to calculate the flow properties at these conditions.

The options used in NEQAIR were as follows:

- Assume Boltzmann distributions
- Line of sight for the geometry
- The gases are well mixed and at thermal and chemical equilibrium
- The volume is that of an infinite slab

The wavelength range under investigation was determined by the species that make up the medium and span from $\tilde{1}60$ nm to $\tilde{1}450$ nm. This range is broken down into 6 surveys and table 4.1 presents the wavelengths and how they are referred to. Additionally, a High-Resolution run was done to study the C_2 Swan band in the red region from 500-520 nm.

The species included in the model are the various product species of CO_2 and N_2, including ions, along with some trace Argon. The radiative contribution of CO_2 is assumed negligable at these temperatures.

Table 4.1: Wavelength ranges for each survey.

Region	Wavelength (nm)
IR	1250-1450
IR2	1050-1250
IR3	850-1050
Red	450-900
Hi-Res Red	500-520
Blue	200-500
VUV	160-220

Ar	CO	N_2
N_2^+	O_2	O_2^+
NO	NO^+	CN
C_2	C	C^+
N	N^+	O
O^+	E^-	

The data from EAST came from three different runs, called shots. Each shot is intended to be run at the same conditions but small differences between shots is inevitable. Therefore, the shock velocity and pressure are recorded with each shot so that proper calculations can be made.

The electronic transitions included were bound-bound, bound-free, and free-free for the three atomic species N, O, and C, and the diatomic systems included were:

N_2 1^+	NO δ	C_2 Swan
N_2 2^+	NO ϵ	CN Red
NO β	NO γ	CN Violet
CO 4^+		

Also, the spectral data was scanned with an internal scanning function which uses a Voigt line shape to approximate the broadening. The parameters for the line shape were provided by EAST facility to match the broadening they saw.

CHAPTER 5

Results

The results are split into two main sections. First, results of the calculations for each diatom are compared with those of Refs. [6, 13, 25, 11]. Then comparisons are made with the EAST data.

5.1 Franck-Condon factors and r-centroids

The five parameter Hulburt-Hirschfelder potential was used to solve for the vibrational energy levels and wavefunctions for all of the band systems of interest. The required spectroscopic constants were taken from various sources and are reported in the following sections.

The percent differences are all given as percentages of the values taken from literature for the comparisons.

The accuracy of the potentials was loosely gauged by comparing the predicted wavelengths of each transition with known values. The database of Robert L. Kurucz [13] was used for the comparisons. Kurucz's tables include rotational levels and are quite extensive; therefore, the values reproduced here were taken at the lowest rotational level available.

5.1.1 C_2 electronic states

The spectroscopic constants reported by Tanabashi et. al. [27] as of 2007 were used for C_2 with the zero point energy used from Hyun's [11] thesis.

The low lying vibrational levels (at or below v'=4 and v"=4) show good agreement with Kurucz's tables, but the higher levels show an increasing under prediction. The largest difference reported in the table is the 6-8 transition followed by the 5-5 transition. This second transition

Table 5.1: C_2 Swan wavelengths (Å)

Transition	Kurucz	QUANTUM
0,0	5167.05	5160.49
0,1	5632.64	5630.61
0,2	6188.63	6185.96
1,0	4753.21	4732.20
1,1	5131.71	5124.56
2,0	4407.40	4376.52
3,5	6002.17	5996.63
4,9	8048.74	8020.55
5,5	5033.74	4663.99
6,8	5890.94	5404.22
9,9	5044.13	4988.98

will also be seen to have a large discrepancy in calculated Franck-Condon factors when compared with Dwivedi[6].

The Franck–Condon factors match quite well for the 5x5 block of vibrational levels 4 and below with the exception of a large percent difference of -27.54% at the 4-0 transition. From there the most outstanding features are a very large percent difference of -512.87% at the 5-5 transition with a FCF of 1.857×10^{-04} and an area along the lower triangular portion of the 5-0 to 8-5 area that also show poor agreement. These values are in the range of 75%-99% different with Franck-Condon factors in the 1×10^{-04} or smaller range for the most part. These extremely small values are a couple of magnitudes smaller than the ones reported by Dwivedi [6].

For the r-centroid comparison, the number of points available in the upper vibrational regions was slim and because they showed more range than the lower lines they were plotted separately. One exception was the v'=4 line which was included with the upper levels because of a large value of ~19%. The largest difference was the 7-3 transition with a difference of -27.25% and FCF of 7.704E-03. They tended to not show much a trend besides sporadic differences.

The v'=1,2,3,5 graph has a slight upward trend to it, but basically just stays within the less than 1% difference for the points available.

The electronic transition moments for the C_2 Swan band system were taken from a study by J. Arnold and S. Langhoff [1]. In this paper, the results were reported as $\sum |R_e|^2$ vs $r(a_0)$; therefore, once the curve for this was found, it was converted to the electronic transition moment function by use of equation 5.1 [11].

$$R_e^2 = \frac{\sum |R_e|^2}{\left(2 - \delta_{0,\Lambda'+\Lambda''}\right)(2S+1)} \tag{5.1}$$

Where (2S+1) is equal to 3 for this transition and Kronecker delta is 0. The final result is an electronic transition moment function of

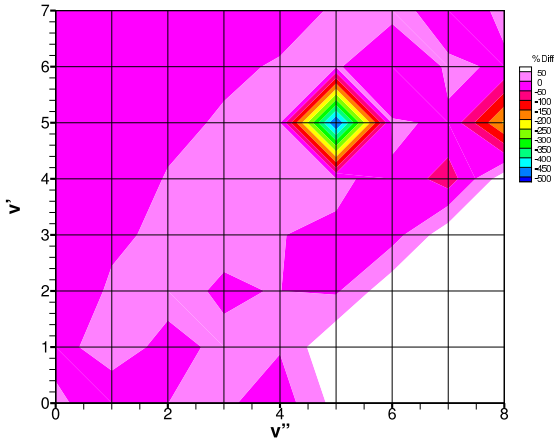

Figure 5.1: Contour plot of % differences for C_2 FCF.

$$R_e = \left(0.13765\bar{r}^2 - 1.6955\bar{r} + 4.004167\right)^{\frac{1}{2}} \tag{5.2}$$

With r-centroids in Bohr radii and the ETMF in atomic units.

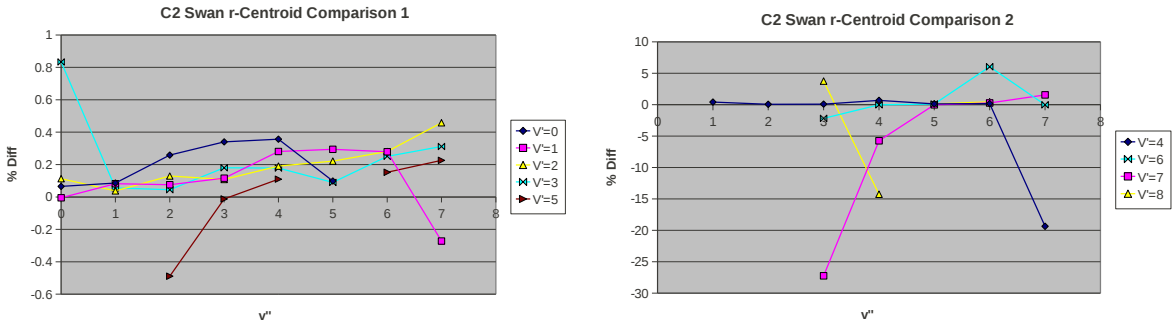

(a) Lower vibrational levels

(b) Upper vibrational levels

Figure 5.2: C_2 Swan band r-centroid comparisons.

5.1.2 CO electronic states

The spectroscopic constants used for the two electronic states were mostly taken from the NIST [10] database with the zero point energy taken from Hyun's [11] thesis.

Table 5.2: CO 4^+ wavelengths (Å).

Transition	Kurucz	QUANTUM
0,0	1544.45	1544.46
0,1	1597.33	1597.33
0,2	1653.24	1653.23
1,0	1509.89	1509.96
1,1	1560.39	1560.46
2,0	1477.6	1477.84
3,5	1705.39	1706.07
4,9	1918.45	1992.8
5,5	1629.78	1631.59
6,8	1763.35	1828.89
9,9	1709.5	1774.95

Most of Kurucz's data is presented in wavelengths (except for the report cited by this paper) so the wavenumbers presented there were converted to wavelengths for the comparison. The first v'=0..5 and v"=0..5 transitions show very good agreement with Kurucz's data, varying at the most by 2-3 Angstroms. As the vibrational levels continue to increase, the differences become greater. The 9-9 transition has a difference of 65 Angstroms (note that this is on the diagonal) and the 4-9 transition shows an even larger difference of 74 Angstroms. These are not necessarily the largest or most significant differences, but they do show the disagreement between transition energies as the vibrational energies increase. Even transitions involving the relatively low state of v'=4, which showed pretty accurate values when the jump went to another low state, was thrown off when the transition occurred to a high vibrational state.

The Franck-Condon factors for the CO 4th positive band were compared to three different papers: Dwivedi et al [6], Silva & Dudeck [25], and Kurucz [13]. The values from Dwivedi were only listed in the range v'=0..9 and v"=0..5, while the others provided a more extensive comparison, reaching the 15th vibrational state in the lower level for both. The latter two, Silva & Dudeck and Kurucz, were compared to the Dwivedi to get a feel for the agreement. There was a maximum discrepancy of a -3359% difference between Dwivedi and Silva & Dudeck and a -4329% difference with Kurucz. These maximums occurred around the 9-5 transition with a FCF on the order of 1.0×10^{-02}. There was also a string of high differences with the 6th and

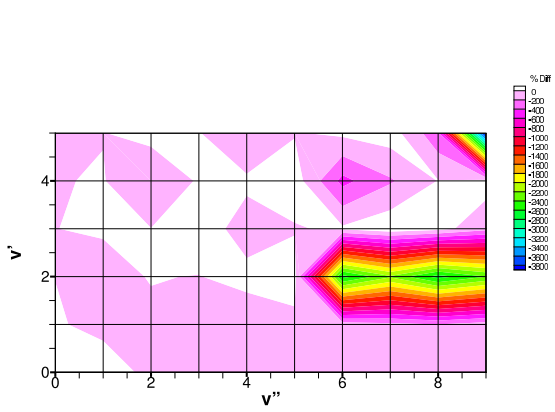

(a) Vs Dwivedi

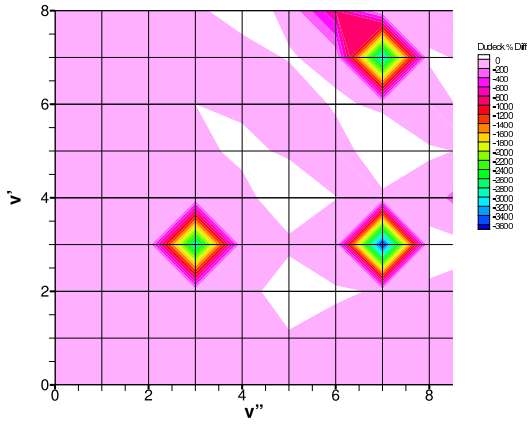

(b) Vs Silva & Dudeck

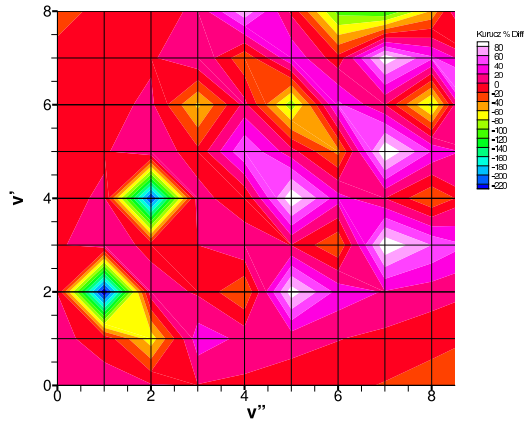

(c) Vs Kurucz

Figure 5.3: Contour plots of % differences for the FCF of the CO 4^+ band system

greater upper states transitioning to the 2nd vibrational level of the lower state.

The newly computed Franck-Condon factors followed a similar trend when compared to the values from Dwivedi et. al. and an even worse comparison to Silva & Dudeck's values. There was a consistent trend with Dwivedi where the higher vibrational states become less similar and the FCFs reached the order of 0.01. The same string of values along the v"=2 lines were off by about 2400% which is about the same as both Kurucz and Silva & Dudeck.

The differences with Silva & Dudeck, however, were more sporadic. They were along the same magnitude as with Dwivedi but showed no trends except being mostly negative. The maximum was around 50000% with two more values of similar magnitude. Two of these do lie outside of the 10x10 range we originally determined to be the most important. The corresponding values for these two points are a FCF of 7.720×10^{-03} and percent difference of-55040% and 2.09×10^{-06} and -24090%. The one inside of the range was at the 3-6 transition with a difference of 20810% and a FCF of 1.654×10^{-01}. After these three, the values drop to within 5000%.

The comparison with Kurucz was better with two main values being very different on the order of -10000% and the next worse being -500%. After those two extreme values, the percent differences drop down to 30% and below for the range of v'=0..15 v"=0..15. The two values occur at 7-6 and 6-11 respectively. Because of this better agreement and the strong interconnectedness of the FCF and r-centroid, the r-centroids from Kurucz were used in the comparison with our computed values.

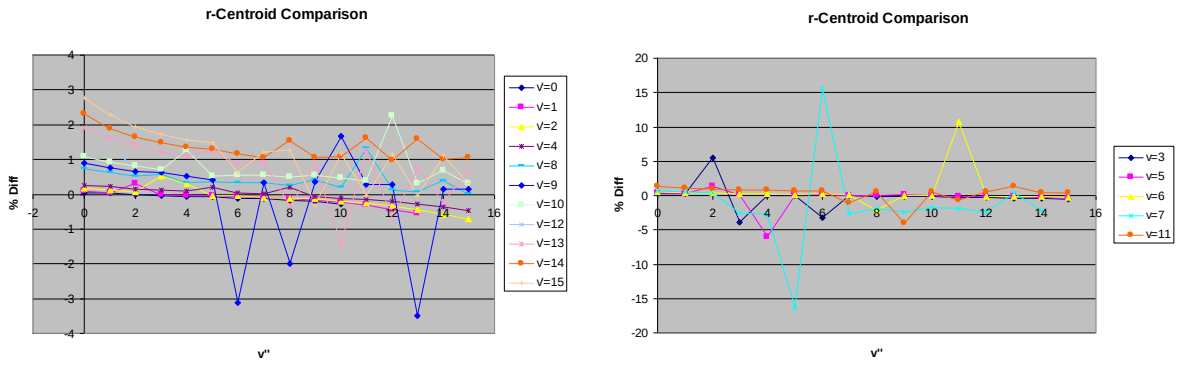

(a) % Differences < 4%

(b) % Differences > 4%

Figure 5.4: A comparison of the new values vs Kurucz's reported r-centroids for the CO 4^+ band system.

Figure 5.4 shows a sample of how our computed r-centroids match up. There is a noticeable trend of our values becoming smaller than Kurucz's as the lower electronic state's vibrational

levels rise, but there is very good agreement between the two. Also, as the upper electronic state's vibrational levels increase, there begins to be more randomness in the differences between the two. The maximum differences were found to be at the 7-5 and 7-6 transitions with a 16 and 15 percent difference, respectively. The FCF for the 7-5 was $5.912{,}9 \times 10^{-06}$ but the 7-6 was $6.770{,}0 \times 10^{-02}$. Compared to the large percent differences found in the FCFs these values are quite close.

The electronic transition moment function was taken from DeLeon [4]. Their data ranged from 1.3 to 1.8 Angstroms and was added to previous data which covered 1.0 to about 1.2 Angstroms. They computed least-squares fit to obtain a quadratic estimate of the ETMF. Their results were:

$$R_e\left(\overline{r}\right) = 10.57\left(41\right)\left[1 - 1.177\left(22\right)\overline{r} + 0.350\left(13\right)\overline{r}^2\right] \tag{5.3}$$

Where, Re is in Debyes and $\bar{r}$ is in Angstroms. The numbers in parentheses are the 1 σ statistical uncertainties given in the paper. Converted into atomic units and Bohr radii, the equation used in this project translates to

$$R_e\left(\overline{r}\right) = 4.158558\left[1 - 0.622841476\overline{r} + 0.09800995\overline{r}^2\right] \tag{5.4}$$

With the coefficients adjusted from what was given without the uncertainties being explored.

5.1.3 CN electronic states

The diatom CN has two band systems over three electronic states included in this project. The plot of the transition shows an example of the potential curves for the two states corresponding to the Violet band system. The Red system would look similar though with a lower lying potential and more vibrational levels in a deeper well.

The constants used for these states match both NIST and Hyun.

Table 5.3 presents the wavelength data for both the Red and Violet band systems of CN. The transitions were kept the same as in all of the previous wavelength comparison tables. The first thing to note is that in table 5.3(a), the result from QUANTUM is negative, similar to Kurucz's line, but showing a jump in energy in the opposite direction. The potential energy curves for the $A^2\Pi_i$ and $X^2\Sigma^+$ states sit very close to each other and, at least as QUANTUM solves for it, the upper vibrational levels of the ground state can overlap with the lower levels of this excited state. This is where the negative number seems to come from. Otherwise the differences in wavelengths are generally low with no real pattern, though the transitions along the diagonal (if these were laid out like a matrix) show a less than one percent difference.

The CN Violet band system showed slightly better results with a slightly more consistant degree of agreement – generally less than a percent difference. A slight pattern was noticed as

Table 5.3: CN Wavelength Tables

(a) CN Red wavelengths (Å)

Transition	Kurucz	QUANTUM
0,0	10927.12	10968.00
0,1	13984.23	14133.90
0,2	19321.84	19764.20
1,0	9144.03	9170.42
1,1	11233.85	11283.60
2,0	7874.84	7895.01
3,5	21831.14	22413.00
4,9	77345.18	-78395.7
5,5	12640.42	12731.50
6,8	25042.81	25758.10
9,9	14424.07	14553.80

(b) CN Violet wavelengths (Å)

Transition	Kurucz	QUANTUM
0,0	3874.61	3876.36
0,1	4200.37	4209.61
0,2	4580.44	4599.89
1,0	3579.96	3581.35
1,1	3862.46	3863.96
2,0	3331.41	3332.14
3,5	4509.61	4520.43
4,9	5955.49	5991.99
5,5	3838.43	3829.61
6,8	4470.80	4459.91
9,9	3870.44	3818.46

the vibrational levels were increased (both along the ground state and the excited state) the computed wavelengths are greater than Kurucz's data while the lower vibrational states were below. Both tables show good agreement between QUANTUM and Kurucz's data.

The Franck-Condon factors for the CN Red system matched to about the same order as the previous systems, with a maximum difference of -917.4% at the 8-6 transition. The next largest differences are found in a group near the low excited state transitioning to the high ground state, v'=0..3 to v"=7..9, and a peak at the 0-5 transition. These values max out at a positive 99% difference and fall off quickly to 50% and below. The rest of the values are 15% or less and usually negative.

The CN Violet band agreed slightly better. There are three values which have been set to zero in figure 5.5(b) due to the tendancy for these values to wash out the plot. They are the 3-8, 8-0, and 8-3 transitions which had values of -22800%, -1090%, and -19500%, respectively. Otherwise the values fall below ±600% and usually within ±50%. There is a slight trend of the values to be greater than the values found in the literature except for transitions from the lower vibrational levels of the upper electronic state to those of the higher vibrational levels of the lower electronic state which show smaller values.

Due to the lack of r-centroid data in Hyun's thesis and the large number of values given by Dwivedi, these were the ones used in the comparison for our calculated values of the Red system. The graph shows a consistent trend of worsening agreement as the ground vibrational level increases; but the first few values, no matter the excited state's vibrational level, all clump together below 0.2% difference. The values in each individual line do not exactly fall linearly but seem to curl slightly upward over the last few values in each. From this data, the lower vibrational levels in the excited state seem to deviate sooner and to a greater extent than the

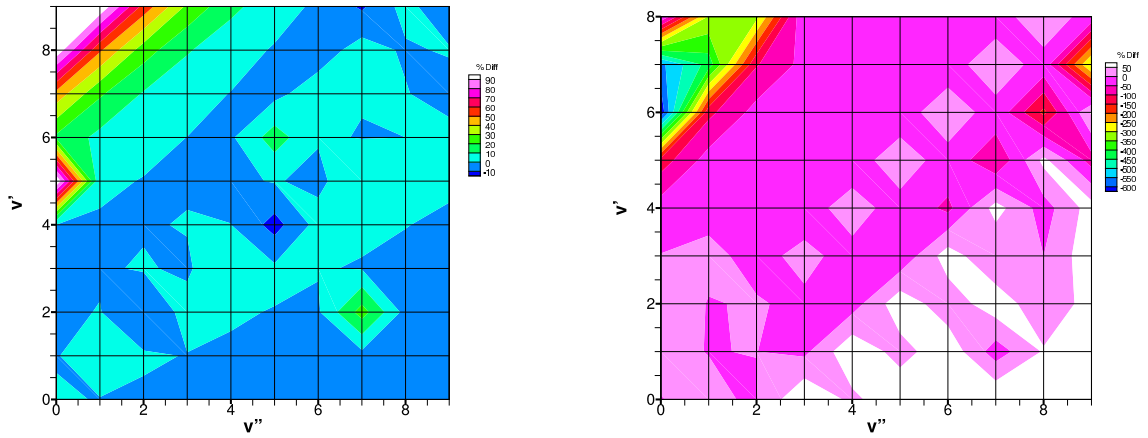

(a) CN Red FCF % diff. contour.

(b) CN Violet FCF % diff. contour

Figure 5.5: CN FCF contours.

higher ones.

These trends can be seen to correspond to the shrinking of the Franck-Condon factors. The v'=0 values get smaller with increasing v" and as they do the r-centroids become more disparate. The size of the FCFs become more consistently in the 1×10^{-02} range in the upper v' levels. It should be noted that for a few extremely low FCFs the r-centroids are extreme. The worst values falling at an r-centroid value of 16.79 and 11.853 with a FCF of 2.846×10^{-12} and 9.369×10^{-13}, respectively. These values are not included in Dwivedi et. al. tables and are left out of the data put into NEQAIR.

There are two plots shown for the CN Violet region because of the large value of -33% on the 6th line, which was paired with the three other largest differences while the other graph shows the ones within 3% difference. There is a slight upward trend among all of the v' constant curves, though the values still center on 0 and there is a large amount of randomness in the lines with the greatest upward component. Overall, the higher v' levels have a larger spread in percentages. They also begin to have fewer points available for comparison.

The major discrepancies fall on three transitions, 6-3 with -33.3%, 8-6 with -11.1%, and 9-6 with-11.25% otherwise the values or less then 10% different. The 6-3 and 9-6 transitions have FCFs of 5.665×10^{-05} and 7.005×10^{-04} which are quite small but the third, 8-6, has a FCF of 1.084×10^{-02}.

The ETMF for both of the CN systems came from the same source, a study done in 1988 by Charles Baushlicher, Stephen Langhoff and Peter Taylor [2]. Using ab initio quantum chemistry

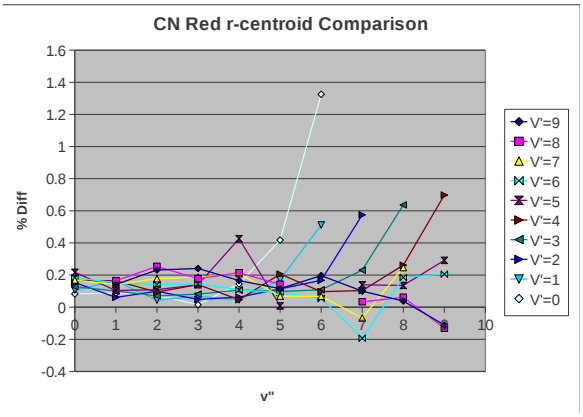

Figure 5.6: CN Red band system r-centroid comparison with values from Ref. [6].

methods they determined the electronic transition moment between the $X^2\Sigma^+$, $A^2\Pi$, and $B^2\Sigma^+$ states of CN over the range of 1.6 to 4.0 Bohr radii. From this data, we were able to perform curve fittings using Microsoft Excel. Both were fit to a cubic equation. The Red system was

$$R_e = 0.039\overline{r}^3 - 0.3624\overline{r}^2 + 0.9683\overline{r} - 0.4922 \tag{5.5}$$
$$R^2 = 0.9993$$

The R^2 value shows this to be a good fit for the data presented. The CN Violet system also had a good R^2 value and was determined to be

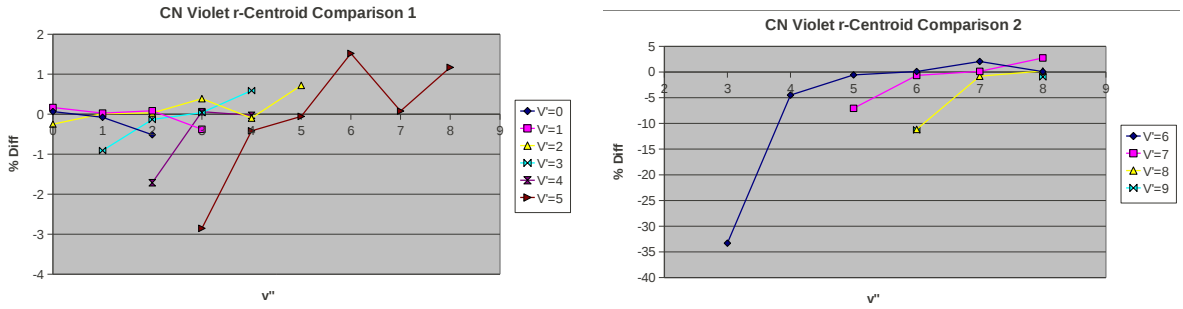

(a) CN low lying vibrational levels.

(b) CN high vibrational levels.

Figure 5.7: CN Violet r-centroid comparisons.

$$R_e = 0.309\overline{r}^3 - 2.7044\overline{r}^2 + 7.327\overline{r} - 5.6492 \tag{5.6}$$
$$R^2 = 0.9863$$

The equations are already in atomic units and Bohr radii so no adjustments were needed for implementation.

The CN Red and CN Violet transition information, similar to the previous two band systems, is located in the appendices. The new data for both systems was limited to v'=0..9 and v"=0..9 because higher vibrational levels have been seen to be less reliable. For the CN Red system the percent differences for the low vibrational levels were at or below 15% while the higher levels showed more sporadic values and switched between increasing and decreasing changes without an apparent trend. The two most notable changes were the 5-6 and 2-8 transitions with 44% and 41% respectively.

The CN Violet band system showed a slight trend of the new probabilities being smaller than the old probabilities, but the differences were still rather small. Here the most notable differences were the 7-5, 8-4, 8-5, and 9-6 transitions with 98%, -56%, -60%, and -53%, respectively. Also, the 7-5, 8-5, and 9-6 all had square root of the transition probabilities that ranged in the 1×10^{-02} range and the 8-4 was even smaller in the 1×10^{-03}.

5.2 EAST Simulations

Finally, the new results were added to NEQAIR and the cases were re-run. The cases were also run using the FCF's reported by Silva & Dudeck [25] as a comparison. They used the RKR potential and were the most up-to-date values available at the time.

5.2.1 Case 1 (VUV Survey)

Due to the fact that the vacuum ultra-violet region is the major contributor to the total radiance for the diatomic electronic transitions, a couple of cases were used in the comparisons. The first case, 7.89 km/s and 0.991 Torr, was an older case used in previous comparisons. This case has a previous prediction shown with each plot to show how the changes have affected the predictions. The second and third cases, are taken from more recent EAST test data. The new data did not contain any cases that matched the previous case with either the pressure being lower or the velocity being higher. Therefore, multiple were selected and the predictions using the current values are shown against test results.

The transition probabilities that had the largest effect in this region were for the CO 4th positive band. The shape shows an overall better match than previous computations with the

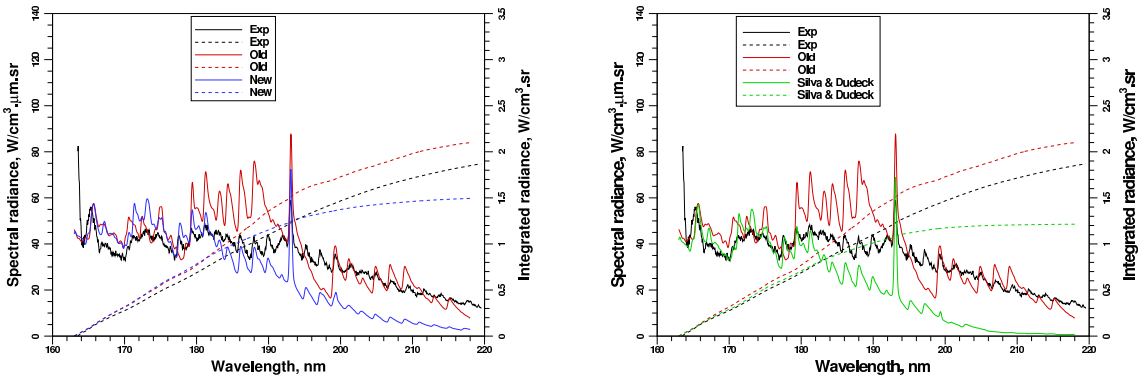

(a) Using New FCFs

(b) Using Silva & Dudeck FCFS

Figure 5.8: NEQAIR 2009 v5 survey of the vacuum ultra-violet region for V = 7.89 km/s P = 0.991 Torr.

region between 165 nm to 180 nm in particular looking more correct. Though a bit high, the feature position and relative magnitudes match the experiment well enough.

After the 180 nm mark though, the newly computed values begin to diverge from the experiment, dropping below the previously computed values as well. The new computation does, however, match the features better than before. The peaks match very well all the way down to just above 210 nm. In particular, directly after the atomic line, the large drop in intensity that is seen in the previous calculations is fixed and the slope looks less sporadic. Overall, the effect was to slightly improve the previous calculations but at a loss of magnitude.

Silva & Dudeck's values give very similar results to those computed using the current method. The predicted spectral features tend to be slightly less than experimental results but the peaks have very similar relative intensities. They also show the same tendency to drop below the experimental values as the wavelengths increase.

The integrated radiance follows the previous calculations, just slightly above the experimental values, until the 180 nm mark where the separation begins. The previous calculations put the integrated radiance at 2.099 W/cm^3·sr and the new ones at 1.467 W/cm^3·sr which is a change of -0.632. This puts the new value 0.4 W/cm^3·sr below the experimental value of 1.87.

A moderate increase in the shock velocity and a doubling of the pressure showed similar results. Both increased the radiative output in this region while preserving the major features. The CO 4th positive band system seems to remain the main contributor in this region for both conditions. The predictions drop below the experimental values a bit faster than in the first case and again the radiance is underpredicted.

The increased velocity had a slightly larger impact on the integrated radiance, but the

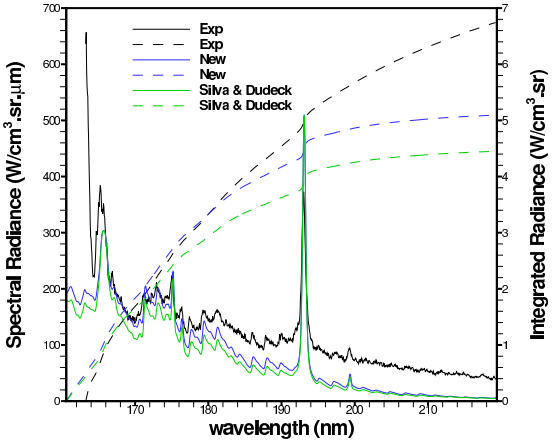

(a) V = 9.49 km/s P 0.99 = Torr.

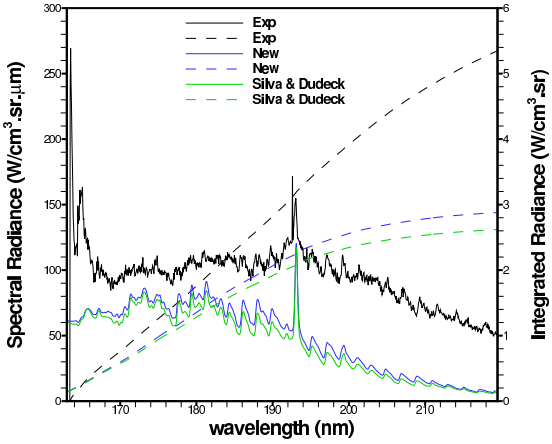

(b) V = 7.68 km/s P = 2.012 Torr.

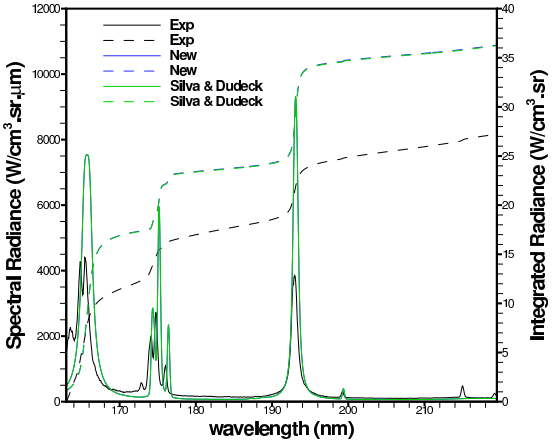

(c) V = 11.85 km/s P = 0.504 Torr.

Figure 5.9: NEQAIR 2009 v5 survey of vacuum ultra-violet region for 3 cases.

doubling in the pressure changed the spectrum shape more significantly. The atomic line becomes less important and the contribution from the band system is proportionaly larger. This caused the predicted values to be worse in the higher pressure case than for the higher velocity case.

The large change in the shock velocity had a large effect on the resulting spectrum. Doubling the speed increased the integrated radiance by an order of magnitude and drastically changed the major features. The CO 4th band system doesn't seem to be as large a contributor as before and the predictions now over-predict the radiation by a significant amount. This seems to be due to the over-prediction of atomic lines in the region. The new features lie in the range of 160-180 nm.

The results using both Silva & Dudeck's values and the presented ones overlap for the highest velocity case, which is to be expected as the band systems become less important and other mechanisms not associated with the FCFS take over.

5.2.2 Case 2 (Blue Survey)

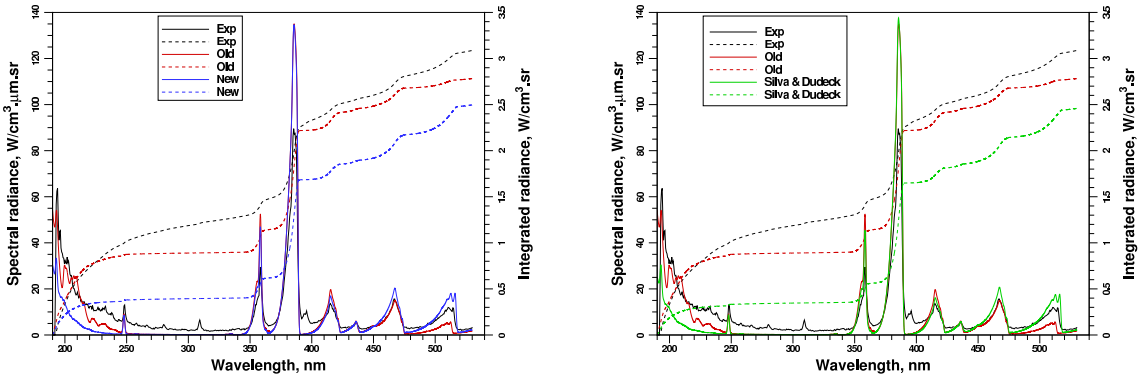

(a) Using New FCFs

(b) Using Silva & Dudeck's FCFs

Figure 5.10: NEQAIR 2009 v5 survey of the blue region for V = 7.89 km/s and P = 0.991 Torr.

The experimental conditions in this region were the same as in the vacuum-ultra violet region with the three extra cases still being shown.

Compared to the previous calculations, this survey showed an overall drop in the integrated radiance. The new values change the shape and magnitude of the features in the left most region which is somewhat to be expected from the previous section. This region 200 to 250 nm includes

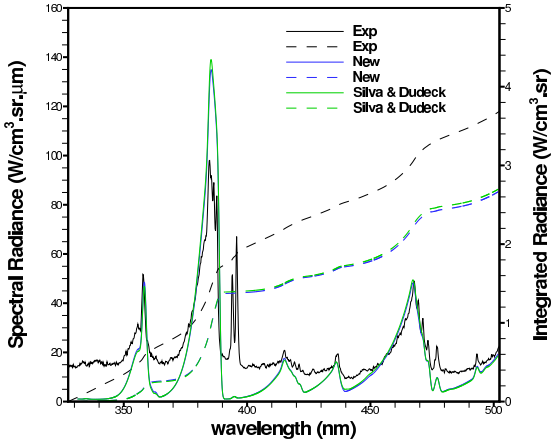

(a) V = 9.49 km/s P 0.99 = Torr.

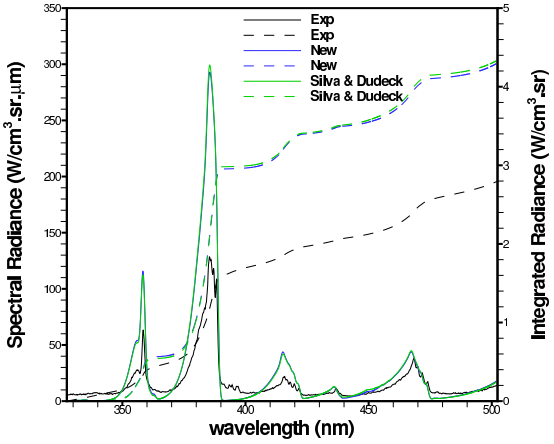

(b) V = 7.68 km/s P = 2.012 Torr.

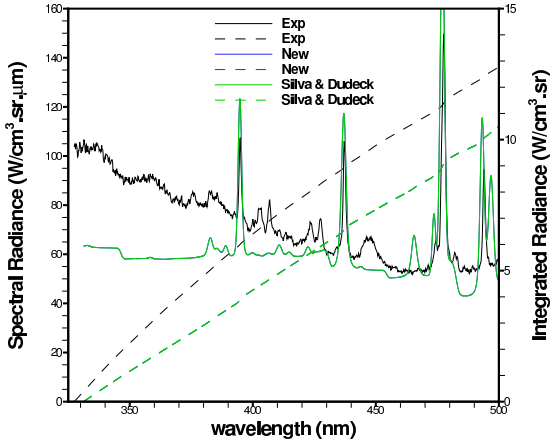

(c) V = 11.85 km/s P = 0.504 Torr.

Figure 5.11: NEQAIR 2009 v5 survey of vacuum ultra-violet region for 3 cases.

about 20 nm of overlap from the blue survey where it was seen that the new computations are predicting much less than the experiment or previous computations. The shape here is a more smooth curvature similar to the experiment as apposed to the previous slope which had an extra feature present.

By the 250 nm mark the old and new values provide very similar results and are about 5 $W/cm^3 \cdot sr$ below the experimental value. The newly computed values alternate with the previous ones in magnitude of features though both show all of the correct peaks in the correct locations. The final shape, was increased quite a bit from previous calculates which pushes the furthest right jump in integrated radiance a little closer to the experimental shape.

As noted above the integrated radiance dropped significantly, mostly attributed to the beginning region. The previous calculations placed this value at 2.783 $W/cm^3 \cdot sr$, approximately 0.3 $W/cm^3 \cdot sr$ less than detected while the new values put the value at 2.5 $W/cm^3 \cdot sr$, a near 0.6 difference.

In this region, Silva & Dudeck's data showed very similar results. If anything the integrated radiance and spectral features were slightly lower than the new values predicted but this difference is mostly negligible.

The increase in shock velocity causes a proportional increase in the radiance in this region with a very noticeable increase in the baseline radiation. The salient features change as the shock velocity increases and the pressure drops and NEQAIR2009 begins to miss more features. The overall affect is to underpredict the radiation in this region.

Doubling the pressure, seems to cause some of the features in this region to be overpredicted by a significant amount and for the integrated radiance to be accordingly overpredicted. The features in this case were similar to those in the first case with very little baseline radiation.

For all cases, the results using the presented values and Silva & Dudeck's values lie on top of each other, performing equally in this region.

5.2.3 Case 3 (Red Survey)

The experimental conditions in this region correspond to a shock traveling at 8.01 km/s and a pressure of 0.992 Torr.

The previous Red survey showed no lack of features, the peaks were in close to the correct place and the new values corrected mainly magnitude issues in the 450 nm to 700 nm span. In particular the peak around the 500 nm mark was greatly increased and nearly matches the experimental value providing the major boost in integrated intensity value. The small humps after the 550 nm region are marginally better in shape and form though still below the reported values and across the board, there seems to be a missing base value of spectral radiance.

The first two peaks have a shallower trough than either prediction catches marking a

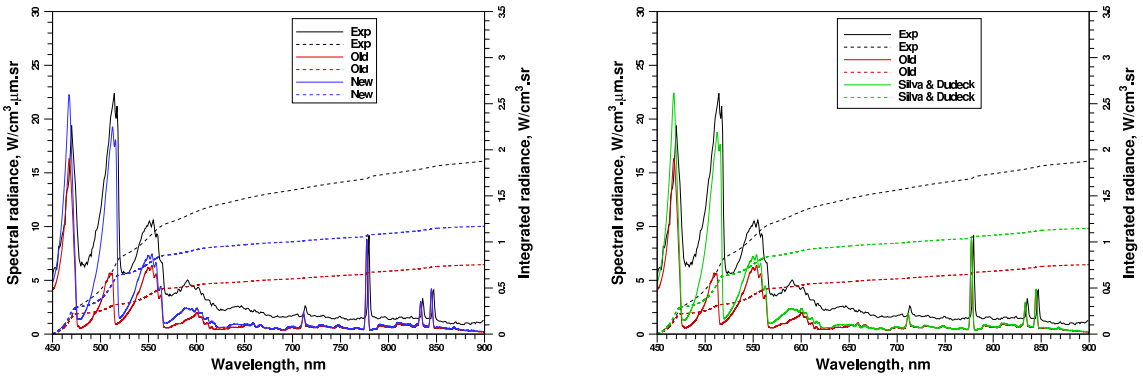

(a) Using New FCFs

(b) Using Silva & Dudeck's FCFs

Figure 5.12: NEQAIR 2009 v5 survey of the red region showing old and new results.

noticeable loss in the integrated value. There is also, still a slight offset in the positioning in the peak locations in the 700 to 850 nm region.

Both sets of new values had about the same effect, though, the ones computed from the wavefunctions provided by QUANTUM resulted in very slightly higher intensities around the 500 nm mark (the C_2 Swan system).

The final result was an increase of 0.416 W/cm^3·sr in the integrated radiance which is still 0.705 W/cm^3·sr below the experimentally determined value of 1.874 W/cm^3·sr.

5.2.4 Case 4 (High Resolution Red Survey)

The high resolution case shown here was taken from a different experimental shot than the full red region. The conditions match those of a shock speed of 8.19 km/s and pressure of 0.993 Torr.

This case showed a large improvement. Two things were actually done to the input file for this region. First, there is an option in NEQAIR to override its computed transition energies with hardcoded values. It was noticed after some searching that two values in the C2 Swan band were supplied and that they were off by a factor of 10 too large. These were removed and NEQAIR was allowed to do all of the computations on its own. This change caused the shift in the band head but left the magnitude the same. The next change was the same one applied to all the other systems. The new square root of the transition probabilities was entered and the older data was removed completely. This caused the correction in the shape and magnitudes. The new plot shows a previous integrated spectral radiance of 0.0741 W/cm^3·sr and a new value of 0.297 W/cm^3·sr. The second value is much closer to the experimental value of 0.3 W/cm^3·sr.

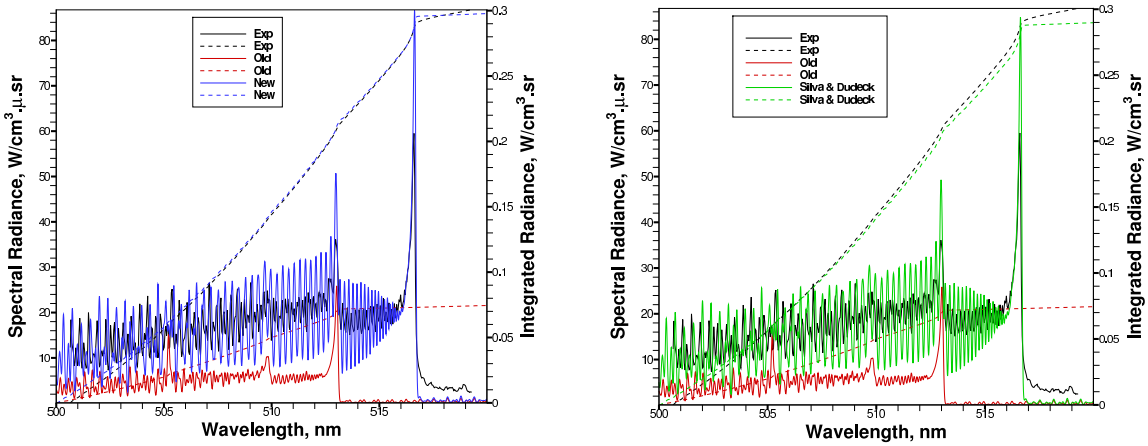

(a) Using New FCFs

(b) Using Silva & Dudeck's FCFs

Figure 5.13: NEQAIR 2009 v5 survey of the Hi-Res red region showing old and new results.

Both Silva & Dudeck and the newly computed values show very similar results. The newly computed FCFs resulted in a slightly higher integrated value which matched the experiment nearly exactly.

The centerline of the spectral radiance follows along the experimental value very well and as can be seen by the integrated values, the overly amplified features match the experimental value in area if not height. The very end shows the computed values flattening out as the spectral radiance drops to near zero while the experimental values continue with a slight noise in this area.

5.2.5 Case 5 (IR Survey)

The infra-red survey was broken down into three smaller runs. Each of the infra-red surveys correspond to different experimental conditions. The IR (1250-1450 nm), IR2 (1050-1250), and IR3 (650-1050) regions correspond to shock velocities of 8.01, 8.19, and 7.89 km/s and pressures of 0.992, 0.993, 0.991 Torr, respectively. The first and third runs will be discussed first because there was little if any change to these regions.

The 850 to 1050 nm range was covered in the IR survey and the changes produced by the new values show a slight increase in integrated radiance, mainly due to slightly shallower valleys between the major peaks in through 900 to 975 range. The shape is still slightly shifted to the left and the 850 to 900 nm range is approximately 0.5 W/cm3*mm*sr too low. There is an obvious dip directly after the peak at the 910 nm mark which is in both computations but does

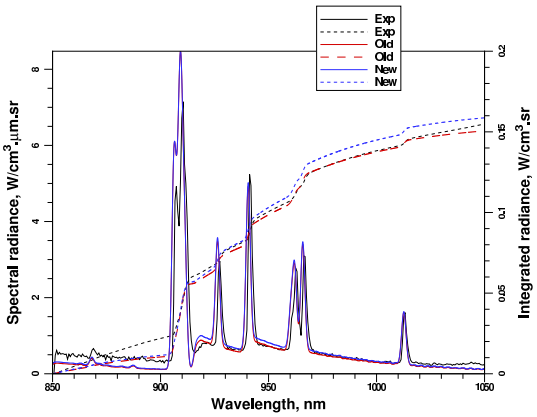

(a) Using New FCFs

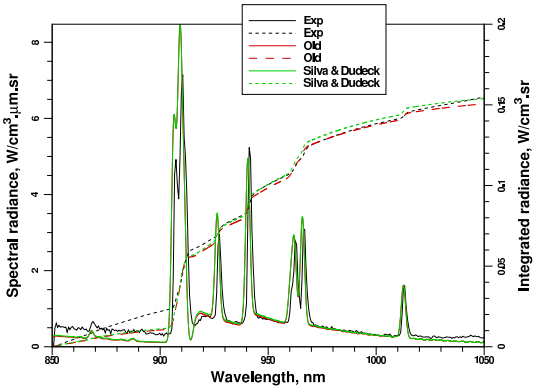

(b) Using Silva & Dudeck's FCFs

Figure 5.14: NEQAIR 2009 v5 Survey of infra-red region, IR (650-1050 nm).

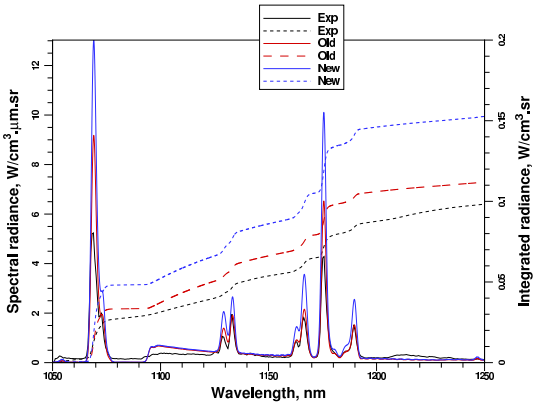

(a) Using new FCFs

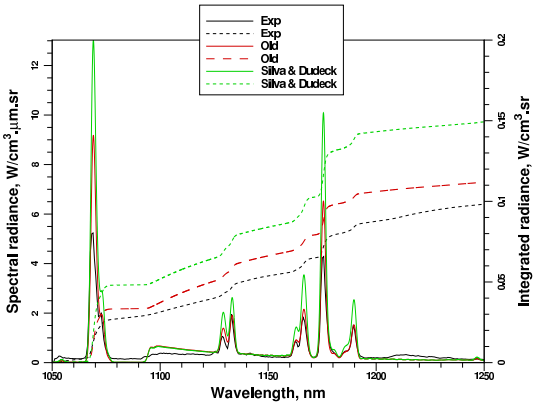

(b) Using Silva & Dudeck's FCFs

Figure 5.15: NEQAIR 2009 v5 survey of infra-red region IR2 (1050-1250 nm).

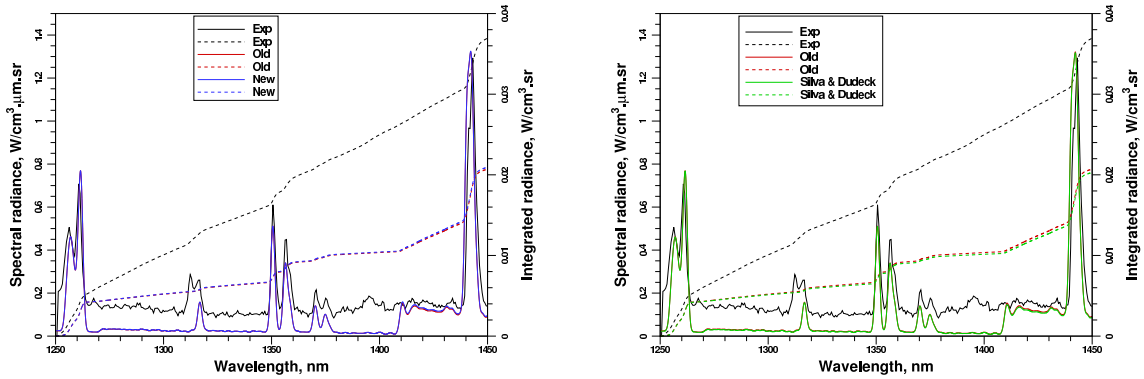

(a) Using new FCFs

(b) Using Silva & Dudeck's FCFs

Figure 5.16: NEQAIR 2009 v5 survey of the infra-read region, IR3 (1250-1450 nm).

not quite match the experimental results.

The final difference in integrated radiance is a 0.006 increase in the computed value making it 0.002 greater than the experimental value instead of 0.004 below.

The values computed using Silva & Dudeck's[25] Franck-Condon factors produced results in agreement with the final value for the experimental integrated radiance over this region.

The IR3 survey showed absolutely no change in computed values. The integrated value is still under predicting by 0.016 W/cm^3·sr. There is still an strange missing base of radiation almost throughout this region except oddly starting after the 1400 nm mark; where NEQAIR jumps up near the experimental values. There is also a missing feature in the 1310 nm wavelength area.

The more interesting range in the Infra-red survey, for these results, is in IR2 which spans 1050 nm to 1250 nm. Though the shape showed no change, no missing or added features, the magnitudes increased noticeably. There was an increase in predicted integrated radiance of 0.0414 W/cm^3·sr putting it above the experimental value by 0.055 W/cm^3·sr. This increase is seen in a jump in all of the peaks, not only the minor peaks caused by the diatomic lines but the atomic lines as well.

In both the IR2 and IR3 surveys, the results using Silva & Dudeck's values give slightly lower results tending to be just below as opposed to just above the integrated radiance line.

CHAPTER 6

Conclusions

Based on the results, the changes to the NEQAIR input successfully moved the C_2 Swan band head location to its theoretical position and changed the shape and magnitude of the spectral radiance to match those reported by the EAST facility. This, in turn, has brought the integrated value very close to experimental results as well. This shows that NEQAIR 2009 v5 can compute the vibrational and rotational energy levels quite well without needing user help and that the new electronic transition moments for the C_2 Swan band system are an improvement over the previous values.

The adjustments to the CO 4th positive system increased the number of features present in the predictions but also caused an underprediction of the radiance and integrated radiance. For the mid to low shock velocities, the diatomic band systems provided the majority of the radiation while for the higher shock velocities the atomic systems were more important. This is expected due to the two orders of magnitude decrease in the diatomic species number densities and the near doubling in temperature for the higher shock velocity case.

The increased pressure caused more output from the diatomic systems and thus lowered the relative contribution from the atomic lines, at least in the vacuum ultra-violet and blue regions. Because of the current descrepencies between experiment and prediction this worsened the results.

The number of transitions for the CO 4th positive band system that needed to be included was upwards of 225 transitions. Meaning a 15x15 matrix is barely sufficient to capture the full shape of the system. Due to the limited range of the Electronic Transition Moment function, not all of the transitions can be included and therefore a larger matrix of possibilities is needed.

The wavelengths from 170 to 190 nm can be provided by the first 100-150 (meaning the 10x10 or 12x12 matrix associated with the possible combinations of the first 10-12 upper and lower vibrational states) transitions while the later peaks are all due to higher and higher vibrational state transitions. Even still, the higher vibrational state transitions also tend to have a broader range in energies and so will affect the lower wavelengths as well. Of course these states will be increasingly rare, but the fact that more than simply the low lying first 10 states makes a difference is significant to note.

The changes to the values the CN Red system do not seem to have brought the predicted values closer to the EAST values. The changes in the infra-red system are too small and inconsistent to be able to attribute them to the new values being either worse or better than the previous. The major discrepancy is still the lack of the continuum radiation which is a major contributor in the infra-red regions.

The Blue region's only change could be attributed to the CO 4th positive system and therefore the adjustment to the CN Violet band system doesn't appear to have any affect either.

One possible source of error is in the integration technique. The adaptive method was devised to help overcome some of these problems but the handling of highly oscillatory integrals, even discrete ones, can be an error prone endeavor and a more advanced method may increase the accuracy. A better integration technique may allow for the inclusion of higher vibrational levels which may increase the accuracy of the finer features.

The shape of the potentials has a very large impact on the integrals, therefore the spectral constants for the electronic states affect the FCFs to a very large degree. An RKR potential is generally considered more accurate than the expansion type potential however these results compared favorably with Silva & Dudeck [25]. The results for the C_2 Swan amd CO 4th positive bands were accurate enough, the CN Violet and Red bands provided too little information to make any conclusions.

Also, all of the calculations have been done assuming an infinite slab at thermal and chemical equilibrium. The flow directly behind the shock wave will most likely not be in chemical or thermal equilibrium and this assumption could possibly account for some of the discrepancies. CEA provides a chemical make-up that is constant for the entire span of the wind tunnel, and NEQAIR thus has the same assumption built in. This means that there is no boundary layer occuring near the wall. This boundary layer would be cooler than the flow along the axis of the tunnel and therefore would have different chemistry. This could easily change the results of the integration along the line of sight as the radiation from the hot center flow passes through and heats the cooler boundary layer. The non-equilibrium species concentrations, a non-boltzmann energy level distribution, and a non-uniform flow field are all possible adjustments that should be investigated to further increase the agreement between NEQAIR 2009 v5 and EAST.

Overall, the adjustment of the C_2 Swan and CO 4th postive band systems provided the

largest changes to the NEQAIR results. Both the new transition probabilities calculated from the wavefunctions provided by QUANTUM[24] and the values of Silva & Dudeck [25] using RKR potentials have increased the agreement between NEQAIR and the experimental data from EAST facility.

REFERENCES

[1] J. O. Arnold and S. R. Langhoff. A theorectical study of the electronic transition moment for the c2 swan band system. *Journal of Quantitative Spectroscy and Radiative Transfer*, 19:461–466, 1978.

[2] Charles W. Bauschlicher, Stephen R. Langhoff, and Peter R. Taylor. Theorectical study of the dissociation energy and the red and violet band systems of cn. *Astrophysical Journal*, 332:531–538, 1988.

[3] Brett A. Cruden, Dinesh Prabhu, Ramon Martinez, Hai Le, Deepak Bose, and J. H. Grinstead. Absolute radiation measurement in venus and mars entry conditions. Number 2010-4508. 10th AIAA/ASME Joint Thermophysics and Heat Transfer Conference, June-July 2010.

[4] R. L. DeLeon. Co (a-x) electric dipole transition moment. *Journal of Chemical Physics*, 89:20–24, 1988.

[5] Dunham. blah for now.

[6] Parmesh H. Dwivedi, David Branch, J. N. Huffaker, and R. A. Bell. Rotational dependence of franck-condon factors for selected band systems of cn, c2, co, and ch. *The Astrophysical Journal Supplement Series*, 36:573–586, 1978.

[7] Victor Gil. *Orbitals in Chemistry: A Modern Guide for Students*. Cambridge University Press, 2000.

[8] Peter A. Gnoffo. Planetary-entry gas dynamics. *Annual Review Fluid Mechanics*, 31:459–494, 1999.

[9] Sanford Gordon and Bonnie J. McBride. *Computer Program for Calculation of Complex Chemical Equilibrium Compositions and Applications*. NASA, June 1996. Reference Publication 1311.

[10] K.P. Huber, G. Herzberg (data prepared by J.W. Gallagher, and III) R.D. Johnson. *NIST Chemistry WebBook, NIST Standard Reference Database Number 69, Eds. P.J. Linstrom and W.G. Mallard*, chapter Constants of Diatomic Molecules. Gaithersburg MD, 20899,, 2010.

[11] Seong-Yoon Hyun. *Radiation Code SPRADIAN07 and Its Applications*. Ph.d. thesis, School of Mechanical, Aerospace, and Systems Engineering, Division of Aerospace Engineering, Korea Advanced Institute of Science and Technology, 2009.

[12] Helge Klemsdal. The variation of the electronic transition moment, re, in the intensity theory of diatomic molecules. *Journal of Quantitative Spectrozcopy and Radiative Transfer*, 13:517–541, 1973.

[13] Robert L. Kurucz. The fourth positive system of carbon monoxide. *SAO Special Report*, 374, 1976.

[14] M. Larsson. Conversion formulas between radiative lifetimes and other dynamical variables for spin-allowed electronic transitions in diatomic molecules. *Astronomy and Astrophysics*, 128:291–298, 1983.

[15] E.R. McCorkle, H.A. Hassan, and M. Barnhardt. Examination of east data using updated shock tube flow. Number 2009-392. AIAA, June 2009.

[16] E.R. McCorkle, H.A. Hassan, B. Cruden, and M. Barnhardt. Role of viscous effects on neqair prediction of east measurements. Number 2010-0236. AIAA, 2010.

[17] Robert S. Mulliken. Role of kinetic energy in the franck-condon principle. *The Journal of Chemical Physics*, 55:309–314, 1971.

[18] M. J. Mumma, E. J. Stone, and E. C. Zipf. Excitation of the co fourth positive band system by electron impact on carbon monoxide and carbon dioxide. *The Journal of Chemical Physics*, 54(6):2627–2634, March 1971.

[19] Chifuru Noda and Richard N. Zare. Relation between classical and quantum formulations of the franck-condon principle: The generalized r-centroid approximation. *Journal of Molecular Spectroscopy*, 95:254–270, 1982.

[20] Chul Park. *Nonequilibrium Hypersonic Aerothermodynamics*. John Wiley & Sons, Inc, 1934.

[21] Chul Park. *Nonequilibrium Air Radiation (NEQAIR) Program: User's Manual*. National Aeronatuics and Space Administration, July 1985.

[22] Chul Park and Hyo-Keun Ahn. Stagnation-point heat transfer rates for pioneer-venus probes. *Journal of Thermophysics and Heat Transfer*, 13(1):33–41, January-March 1999.

[23] W. C. Pitts and R. M. Wakefield. Performance of entry heat shields on pioneer venus probes. *Journal of Geophysical Research*, 85(A13):8333–8337, December 1980.

[24] Dinesh Prabhu. *Vibrational energies of diatomic molecules using the finite-element method*. National Aerospace Laboratories, Bangalore 560 017 India, June 1995.

[25] M. Lino da Silva and M. Dudeck. Arrays of radiative transition probabilities for co_2-n_2 plasmas. *Journal of Quantitative Spectrscopy and Radiative Transfer*, 102:348–386, 2006.

[26] Hughes Aircraft Company Space and Communications Group. Pioneer-venus: Case study in spacecraft design. AIAA professional study series, 1979.

[27] A. Tanabashi, T. Hirao, T. Amano, and P. F. Bernath. The swan system of c2: A global analysis of fourier transform emission spectra. *the Astrophysical Journal Supplement Series*, 169:472–484, 2007.

[28] Walter G. Vincenti and Jr. Charles H. Kruger. *Introduction to Physical Gas Dynamics*. Krieger Publishing Company, 1965.

[29] Ya. B. Zel'dovich and Yu. P. Raizer. *Physics of Shock Waves and High-Temperature Hydrodynamic Phenomena*. Academic Press, 1966.

APPENDICES

APPENDIX A

Spectroscopic Contants

Table A.1: C_2 Spectroscopic Constants from Tanabashi et al. [27] & Hyun[11]

C_2	$\mu =$	6.01E-003						
	T_e	D_0	ω_e	$\omega_e x_e$	$\omega_e y_e$	$\omega_e z_e$	r_e	α_e
$a^3\Pi_u$	716.24	49500	1641.341	1.17E+001	-8.30E-004	0.00E+000	1.3119	0.01657
$d^3\Pi_g$	20022.5	30120	1789.094	1.74E+001	-1.36E-001	-4.88E-002	1.2651	0.0196

Table A.2: CO Spectroscopic Constants from NIST [10] & Hyun [11]

CO	$\mu =$	6.86E-003						
	T_e	D_0	ω_e	$\omega_e x_e$	$\omega_e y_e$	$\omega_e z_e$	r_e	α_e
$A^1\Pi$	65075.77	24740	1.52E+003	1.94E+001	7.66E-001	0.00E+000	1.2353	0.02325
$X^1\Sigma^+$	0	89490	2.17E+003	1.33E+001	1.05E-002	0.00E+000	1.1283	0.0175

Table A.3: CN Spectroscopic Constants from NIST [10] & Hyun [11]

CN	$\mu =$	6.46E-003						
	T_e	D_0	ω_e	$\omega_e x_e$	$\omega_e y_e$	$\omega_e z_e$	r_e	α_e
$B^2\Sigma^+$	25752.8	55130	2.16E+003	1.81E+001	-4.31E-001	0.00E+000	1.1511	0.02005
$A^2\Pi_i$	9245.28	52580	1.81E+003	1.26E+001	0.00E+000	0.00E+000	1.2333	0.01708
$X^2\Sigma^+$	0	61631	2.07E+003	1.31E+001	-9.09E-003	0.00E+000	1.1718	0.01736

APPENDIX B

CEA Results for Corresponding EAST Experments

Table B.1: Species Number Densities and Temperatures to Match Shot 1.

Shot 01 Vel = 8.01 km/s Press = 0.992 Torr Temp = 7313.2 K

Total	1.38E+018						
Ar	1.92E+014	CO	3.33E+017	N2	1.17E+015	N2+	7.55E+010
O2	2.43E+014	O2+	9.95E+011	NO	5.08E+014	NO+	3.91E+013
CN	7.09E+014	C2	2.89E+014	C	2.17E+017	C+	2.47E+015
N	4.86E+016	N+	1.07E+013	O	7.73E+017	O+	1.51E+014
E-	2.84E+015						

Table B.2: Species Number Densities and Temperatures to Match Shot 8.

Shot 08 Vel = 8.19 km/s Press = 0.993 Torr Temp = 7419 K

Total	1.42E+018						
Ar	2.01E+014	CO	3.09E+017	N2	9.73E+014	N2+	7.62E+010
O2	2.39E+014	O2+	1.08E+012	NO	4.69E+014	NO+	3.74E+013
CN	6.96E+014	C2	3.28E+014	C	2.46E+017	C+	3.04E+015
N	4.96E+016	N+	1.27E+013	O	8.09E+017	O+	1.81E+014
E-	3.45E+015						

Table B.3: Species Number Densities and Temperatures to Match Shot 9.

Shot 09 Vel = 7.89 km/s Press = 0.991 Torr Temp = 7243 K

Total	1.35E+018						
Ar	1.87E+014	CO	3.49E+017	N2	1.32E+015	N2+	7.50E+010
O2	2.45E+014	O2+	9.43E+011	NO	5.35E+014	NO+	4.03E+013
CN	7.13E+014	C2	2.62E+014	C	1.97E+017	C+	2.14E+015
N	4.78E+016	N+	9.49E+012	O	7.49E+017	O+	1.34E+014
E-	2.48E+015						

Table B.4: Species Number Densities and Temperatures to Match Test 49 Shot 01.

Shot 01 Vel = 9.49 km/s Press = 0.99 Torr Temp = 8400.9 K

Total	1.69E+018						
Ar	1.95E+014	CO	9.93E+016	N2	1.90E+014	N2+	8.58E+010
O2	1.69E+014	O2+	2.03E+012	NO	2.04E+014	NO+	2.60E+013
CN	3.70E+014	C2	4.01E+014	C	4.59E+017	C+	1.30E+016
N	5.40E+016	N+	5.76E+013	O	1.04E+018	O+	8.40E+014
E-	1.39E+016						

Table B.5: Species Number Densities and Temperatures to Match Test 49 Shot 19.

Shot 19 Vel = 11.85 km/s Press = 0.504 Torr Temp = 12185 K

Total	9.14E+017						
Ar	8.65E+013	CO	1.47E+014	N2	4.42E+011	N2+	4.52E+010
O2	5.03E+012	O2+	2.20E+012	NO	2.52E+012	NO+	3.10E+012
CN	2.29E+012	C2	4.31E+012	C	1.55E+017	C+	9.89E+016
N	2.24E+016	N+	2.08E+015	O	4.82E+017	O+	2.64E+016
E-	1.27E+017						

Table B.6: Species Number Densities and Temperatures to Match Test 49 Shot 25.

Shot 25 Vel = 7.68 km/s Press = 2.01 Torr Temp = 7361.4 K

Total	2.55E+018						
Ar	3.63E+014	CO	7.54E+017	N2	3.76E+015	N2+	2.31E+011
O2	7.35E+014	O2+	2.75E+012	NO	1.60E+015	NO+	1.09E+014
CN	1.76E+015	C2	5.51E+014	C	3.08E+017	C+	3.18E+015
N	9.17E+016	N+	1.88E+013	O	1.38E+018	O+	2.50E+014
E-	3.56E+015						

Table B.7: Survey to Shot Matchup

Shot 01	red, IR
Shot 08	IR2, Hi-Res red
Shot 09	IR3, blue, VUV
Test 49 Shot 01	VUV, blue
Test 49 Shot 19	VUV, blue
Test 49 Shot 25	VUV, blue

APPENDIX C

Franck-Condon Factors and r-Centroids

Table C.1: C_2 Swan: Franck-Condon factor, r-centroid (Bohr)

v' \ v"	0	1	2	3	4	5	6	7	8	9
0	7.2054E-01	2.2141E-01	4.7548E-02	8.7238E-03	1.4820E-03	2.4308E-04	3.9468E-05	6.4372E-06	1.0616E-06	1.7688E-07
	2.4445E+00	2.3148E+00	2.2108E+00	2.1178E+00	2.0325E+00	1.9536E+00	1.8804E+00	1.8119E+00	1.7464E+00	1.6812E+00
1	2.5066E-01	3.3409E-01	2.8200E-01	1.0035E-01	2.5821E-02	5.6638E-03	1.1411E-03	2.2002E-04	4.1593E-05	7.8105E-06
	2.5852E+00	2.4705E+00	2.3283E+00	2.2234E+00	2.1304E+00	2.0455E+00	1.9669E+00	1.8938E+00	1.8252E+00	1.7598E+00
2	2.7873E-02	3.7366E-01	1.3264E-01	2.6263E-01	1.3924E-01	4.7169E-02	1.2820E-02	3.0824E-03	6.9109E-04	1.4902E-04
	2.7644E+00	2.6050E+00	2.5093E+00	2.3416E+00	2.2355E+00	2.1424E+00	2.0579E+00	1.9797E+00	1.9068E+00	1.8383E+00
3	9.2668E-04	6.8060E-02	4.2160E-01	3.9709E-02	2.1178E-01	1.5907E-01	6.8167E-02	2.2304E-02	6.2637E-03	1.6063E-03
	3.0639E+00	2.7875E+00	2.6264E+00	2.5861E+00	2.3546E+00	2.2471E+00	2.1538E+00	2.0697E+00	1.9919E+00	1.9193E+00
4	6.2314E-07	2.7651E-03	1.1119E-01	4.2953E-01	5.7161E-03	1.5577E-01	1.6194E-01	8.5384E-02	3.2908E-02	1.0613E-02
	6.0845E+00	3.1155E+00	2.8119E+00	2.6496E+00	2.8522E+00	2.3671E+00	2.2582E+00	2.1645E+00	2.0808E+00	2.0035E+00
5	7.2350E-07	2.1487E-08	4.9888E-03	1.5207E-01	4.1981E-01	1.8571E-04	1.0682E-01	1.5277E-01	9.7035E-02	4.3294E-02
	2.7271E+00	-3.2735E+01	3.1778E+00	2.8379E+00	2.6753E+00	1.8173E-02	2.3786E+00	2.2688E+00	2.1743E+00	2.0911E+00
6	4.5219E-09	4.5240E-06	1.1151E-05	6.8687E-03	1.8803E-01	4.0614E-01	5.5143E-03	6.8966E-02	1.3676E-01	1.0281E-01
	4.4572E+00	2.8573E+00	4.5172E-01	3.2566E+00	2.8658E+00	2.7035E+00	1.9546E+00	2.3876E+00	2.2792E+00	2.1831E+00
7	1.2764E-09	3.8343E-09	1.5143E-05	8.8724E-05	7.7040E-03	2.1767E-01	3.9661E-01	1.2322E-02	4.2016E-02	1.1817E-01
	2.6903E+00	7.6457E+00	2.9872E+00	1.7462E+00	3.3634E+00	2.8960E+00	2.7344E+00	2.0655E+00	2.3906E+00	2.2895E+00
8	1.1682E-12	1.2135E-08	1.7561E-08	3.4825E-05	3.5201E-04	7.0258E-03	2.3986E-01	3.9593E-01	1.6234E-02	2.4008E-02
	8.5598E+00	2.8994E+00	-1.5108E+00	3.1312E+00	2.2251E+00	3.5247E+00	2.9289E+00	2.7677E+00	2.0405E+00	2.3789E+00
9	4.1178E-12	3.1182E-11	5.4534E-08	4.8195E-07	5.8650E-05	9.8329E-04	4.8305E-03	2.5308E-01	4.0677E-01	1.5842E-02
	3.0050E+00	-5.5394E-01	3.1160E+00	1.5599E+00	3.3142E+00	2.4919E+00	3.8173E+00	2.9652E+00	2.8029E+00	1.9203E+00

Table C.2: CO 4th Positive: Franck-Condon factor, r-centroid (Bohr)

v'\v"	0	1	2	3	4	5	6	7	8	9	10	11	12	13	14	15	16	17	18	19
0	1.1323E-01	2.6149E-01	2.8552E-01	1.9624E-01	9.5438E-02	3.5040E-02	1.0125E-02	2.3712E-03	4.6013E-04	7.5258E-05	1.0515E-05	1.2697E-06	1.3399E-07	1.2403E-08	9.9748E-10	7.2703E-11	5.0780E-12	2.6509E-13	1.8355E-14	2.8336E-16
	2.2314E+00	2.2868E+00	2.3427E+00	2.3993E+00	2.4564E+00	2.5142E+00	2.5724E+00	2.6311E+00	2.6899E+00	2.7489E+00	2.8082E+00	2.8674E+00	2.9262E+00	2.9857E+00	3.0507E+00	3.1047E+00	3.1393E+00	3.2918E+00	3.0707E+00	1.6153E+00
1	2.1616E-01	1.5450E-01	2.9218E-03	7.7430E-02	1.9418E-01	1.8547E-01	1.0748E-01	4.3969E-02	1.3679E-02	3.3845E-03	6.8622E-04	1.1651E-04	1.6837E-05	2.0986E-06	2.2745E-07	2.1480E-08	1.8162E-09	1.4350E-10	7.9831E-12	2.7982E-13
	2.1932E+00	2.2471E+00	2.2911E+00	2.3613E+00	2.4164E+00	2.4728E+00	2.5300E+00	2.5876E+00	2.6457E+00	2.7039E+00	2.7623E+00	2.8209E+00	2.8795E+00	2.9380E+00	2.9969E+00	3.0583E+00	3.1147E+00	3.1526E+00	3.2919E+00	3.5685E+00
2	2.2993E-01	1.2035E-02	9.0017E-02	1.1540E-01	4.8321E-03	5.7971E-02	1.6537E-01	1.6633E-01	9.9336E-02	4.1515E-02	1.3147E-02	3.3072E-03	6.8181E-04	1.1779E-04	1.7334E-05	2.2000E-06	2.4305E-07	2.3650E-08	2.0345E-09	1.4571E-10
	2.1565E+00	2.2058E+00	2.2670E+00	2.3198E+00	2.3659E+00	2.4351E+00	2.4898E+00	2.5463E+00	2.6033E+00	2.6607E+00	2.7184E+00	2.7762E+00	2.8341E+00	2.8921E+00	2.9502E+00	3.0084E+00	3.0672E+00	3.1250E+00	3.1818E+00	3.2662E+00
3	1.8121E-01	2.0503E-02	1.1600E-01	6.2164E-04	8.9240E-02	8.3791E-02	4.7677E-04	6.6975E-02	1.5749E-01	1.4833E-01	8.5692E-02	3.5170E-02	1.1041E-02	2.7715E-03	5.7309E-04	9.9697E-05	1.4820E-05	1.9044E-06	2.1362E-07	2.1083E-08
	2.1213E+00	2.1786E+00	2.2289E+00	2.2530E+00	2.3398E+00	2.3925E+00	2.4162E+00	2.5081E+00	2.5632E+00	2.6195E+00	2.6763E+00	2.7334E+00	2.7906E+00	2.8478E+00	2.9052E+00	2.9627E+00	3.0203E+00	3.0782E+00	3.1364E+00	3.1939E+00
4	1.1874E-01	8.6891E-02	3.4063E-02	5.6681E-02	6.6176E-02	5.8816E-03	9.7139E-02	5.2344E-02	2.1431E-03	8.5064E-02	1.5381E-01	1.3039E-01	7.1110E-02	2.8201E-02	8.6772E-03	2.1559E-03	4.4437E-04	7.7467E-05	1.1587E-05	1.5030E-06
	2.0875E+00	2.1420E+00	2.1919E+00	2.2504E+00	2.3005E+00	2.3674E+00	2.4125E+00	2.4652E+00	2.5382E+00	2.5811E+00	2.6364E+00	2.6925E+00	2.7489E+00	2.8055E+00	2.8621E+00	2.9189E+00	2.9757E+00	3.0327E+00	3.0900E+00	3.1476E+00
5	6.8833E-02	1.2235E-01	2.9673E-04	8.9733E-02	4.3117E-05	8.0690E-02	2.3741E-02	2.9356E-02	9.4088E-02	2.3981E-02	1.4029E-02	1.0425E-01	1.4804E-01	1.1242E-01	5.7562E-02	2.1964E-02	6.6023E-03	1.6196E-03	3.3210E-04	5.7929E-05
	2.0550E+00	2.1085E+00	2.1910E+00	2.2142E+00	2.1454E+00	2.3222E+00	2.3711E+00	2.4345E+00	2.4855E+00	2.5374E+00	2.6021E+00	2.6540E+00	2.7093E+00	2.7650E+00	2.8209E+00	2.8770E+00	2.9331E+00	2.9893E+00	3.0458E+00	3.1024E+00
6	3.6686E-02	1.1547E-01	3.1254E-02	4.2121E-02	4.0585E-02	4.3105E-02	1.9421E-02	7.3175E-02	1.3479E-03	5.8389E-02	7.6236E-02	5.3439E-03	3.4128E-02	1.1945E-01	1.3873E-01	9.5247E-02	4.5944E-02	1.6897E-02	4.9676E-03	1.2040E-03
	2.0238E+00	2.0766E+00	2.1312E+00	2.1799E+00	2.2373E+00	2.2851E+00	2.3466E+00	2.3945E+00	2.4277E+00	2.5063E+00	2.5587E+00	2.6067E+00	2.6733E+00	2.7268E+00	2.7817E+00	2.8370E+00	2.8925E+00	2.9480E+00	3.0036E+00	3.0594E+00
7	1.8450E-02	8.7833E-02	7.1803E-02	2.5735E-03	7.1604E-02	6.1278E-06	6.7694E-02	4.4379E-03	5.3366E-02	4.2261E-02	5.7854E-03	7.7612E-02	4.9921E-02	7.0559E-05	5.7382E-02	1.2829E-01	1.2673E-01	7.9774E-02	3.6522E-02	1.3008E-02
	1.9938E+00	2.0461E+00	2.0992E+00	2.1415E+00	2.2033E+00	1.9282E+00	2.3086E+00	2.3488E+00	2.4171E+00	2.4668E+00	2.5333E+00	2.5792E+00	2.6317E+00	2.7579E+00	2.7454E+00	2.7992E+00	2.8538E+00	2.9086E+00	2.9635E+00	3.0185E+00
8	8.9199E-03	5.8456E-02	8.9337E-02	8.6463E-03	4.5094E-02	2.8664E-02	3.2329E-02	2.5308E-02	4.6327E-02	5.5232E-03	6.7022E-02	1.2119E-02	2.8039E-02	7.9712E-02	2.4806E-02	6.8263E-03	7.8852E-02	1.3077E-01	1.1362E-01	6.6572E-02
	1.9649E+00	2.0169E+00	2.0692E+00	2.1249E+00	2.1715E+00	2.2282E+00	2.2738E+00	2.3338E+00	2.3805E+00	2.4468E+00	2.4898E+00	2.5378E+00	2.6014E+00	2.6525E+00	2.7041E+00	2.7684E+00	2.8177E+00	2.8713E+00	2.9254E+00	2.9797E+00
9	4.2038E-03	3.5629E-02	8.3593E-02	3.7538E-02	9.4189E-03	5.7100E-02	1.4164E-04	5.6161E-02	4.7036E-04	5.4426E-02	1.1824E-02	3.2093E-02	5.3572E-02	5.6483E-05	5.2330E-02	6.7426E-02	7.7064E-03	2.1089E-02	9.5529E-02	1.2834E-01
	1.9370E+00	1.9890E+00	2.0408E+00	2.0935E+00	2.1399E+00	2.1962E+00	2.1798E+00	2.2992E+00	2.3108E+00	2.4050E+00	2.4505E+00	2.5137E+00	2.5632E+00	2.5305E+00	2.6739E+00	2.7257E+00	2.7745E+00	2.8382E+00	2.8897E+00	2.9430E+00
10	1.9521E-03	2.0473E-02	6.6238E-02	6.1117E-02	6.2717E-04	4.5760E-02	1.8083E-02	2.8372E-02	2.4089E-02	3.0789E-02	1.4711E-02	4.8655E-02	1.7148E-04	5.4260E-02	2.8290E-02	7.0407E-03	6.7488E-02	4.8524E-02	4.7828E-04	3.7878E-02
	1.9102E+00	1.9621E+00	2.0137E+00	2.0655E+00	2.1301E+00	2.1668E+00	2.2234E+00	2.2669E+00	2.3260E+00	2.3708E+00	2.4324E+00	2.4781E+00	2.5895E+00	2.5867E+00	2.6365E+00	2.6998E+00	2.7471E+00	2.7985E+00	2.8277E+00	2.9097E+00
11	9.0075E-04	1.1312E-02	4.7183E-02	6.8940E-02	1.5294E-02	1.7682E-02	4.3503E-02	1.1051E-03	4.6883E-02	7.8961E-05	4.7498E-02	2.6482E-03	4.1606E-02	2.2431E-02	1.3504E-02	5.7285E-02	8.1570E-03	2.3848E-02	7.0819E-02	3.0159E-02
	1.8843E+00	1.9364E+00	1.9878E+00	2.0391E+00	2.0919E+00	2.1387E+00	2.1932E+00	2.2194E+00	2.2942E+00	2.2469E+00	2.3977E+00	2.4339E+00	2.5037E+00	2.5512E+00	2.6129E+00	2.6606E+00	2.7078E+00	2.7702E+00	2.8202E+00	2.8708E+00
12	4.1587E-04	6.0982E-03	3.1309E-02	6.3758E-02	3.5589E-02	1.2113E-03	4.3878E-02	8.6880E-03	2.8330E-02	1.8516E-02	2.4441E-02	1.6868E-02	3.3749E-02	5.1731E-03	4.8566E-02	3.1777E-03	3.4154E-02	4.5106E-02	2.0735E-04	4.0802E-02
	1.8593E+00	1.9117E+00	1.9631E+00	2.0142E+00	2.0656E+00	2.1071E+00	2.1661E+00	2.2240E+00	2.2646E+00	2.3232E+00	2.3660E+00	2.4264E+00	2.4711E+00	2.5354E+00	2.5778E+00	2.6195E+00	2.6853E+00	2.7347E+00	2.7481E+00	2.8430E+00
13	1.9321E-04	3.2426E-03	1.9814E-02	5.2140E-02	4.9262E-02	2.9899E-03	2.5686E-02	2.9398E-02	4.1091E-03	3.8397E-02	3.9801E-04	3.9962E-02	1.0160E-03	3.8947E-02	9.2017E-03	2.5120E-02	3.5438E-02	1.0366E-03	4.7728E-02	2.8329E-02
	1.8353E+00	1.8881E+00	1.9396E+00	1.9905E+00	2.0413E+00	2.0956E+00	2.1408E+00	2.1945E+00	2.2311E+00	2.2937E+00	2.3010E+00	2.3952E+00	2.4211E+00	2.4990E+00	2.5433E+00	2.6048E+00	2.6525E+00	2.7249E+00	2.7594E+00	2.8084E+00
14	9.0761E-05	1.7154E-03	1.2159E-02	3.9327E-02	5.3237E-02	1.5159E-02	7.7275E-03	3.7992E-02	1.8925E-03	2.9851E-02	1.0721E-02	2.3682E-02	1.3204E-02	2.7033E-02	7.2377E-03	3.7963E-02	2.4621E-06	3.9978E-02	1.7441E-02	1.0304E-02
	1.8120E+00	1.8654E+00	1.9172E+00	1.9680E+00	2.0186E+00	2.0699E+00	2.1163E+00	2.1696E+00	2.2351E+00	2.2670E+00	2.3260E+00	2.3665E+00	2.4264E+00	2.4693E+00	2.5311E+00	2.5741E+00	3.0337E+00	2.6795E+00	2.7269E+00	2.7872E+00
15	4.3285E-05	9.0896E-04	7.3250E-03	2.8100E-02	4.9752E-02	2.8181E-02	1.7469E-04	3.0775E-02	1.5133E-02	1.0011E-02	2.8561E-02	2.3676E-03	3.2388E-02	1.7170E-03	3.2444E-02	6.1523E-03	2.5279E-02	2.2146E-02	6.6690E-03	4.2183E-02
	1.7897E+00	1.8438E+00	1.8958E+00	1.9468E+00	1.9971E+00	2.0477E+00	2.0824E+00	2.1467E+00	2.2010E+00	2.2402E+00	2.2980E+00	2.3299E+00	2.3977E+00	2.4291E+00	2.4997E+00	2.5416E+00	2.6033E+00	2.6497E+00	2.7104E+00	2.7550E+00
16	2.1031E-05	4.8518E-04	4.3731E-03	1.9372E-02	4.2354E-02	3.6717E-02	2.6446E-03	1.7016E-02	2.7017E-02	1.9245E-04	2.9783E-02	3.2104E-03	2.5413E-02	6.5790E-03	2.5755E-02	4.5775E-03	3.1691E-02	1.4448E-04	3.4998E-02	7.7200E-03
	1.7681E+00	1.8231E+00	1.8756E+00	1.9267E+00	1.9770E+00	2.0271E+00	2.0794E+00	2.1254E+00	2.1777E+00	2.1750E+00	2.2740E+00	2.3378E+00	2.3722E+00	2.4332E+00	2.4731E+00	2.5355E+00	2.5760E+00	2.6789E+00	2.6795E+00	2.7242E+00
17	1.0441E-05	2.6208E-04	2.6065E-03	1.3057E-02	3.3881E-02	3.9660E-02	1.0153E-02	5.7146E-03	2.9364E-02	3.7069E-03	1.7607E-02	1.6300E-02	7.6910E-03	2.2761E-02	5.0980E-03	2.3749E-02	8.0870E-03	1.8946E-02	1.8719E-02	6.6987E-03
	1.7475E+00	1.8034E+00	1.8565E+00	1.9078E+00	1.9581E+00	2.0080E+00	2.0584E+00	2.1052E+00	2.1571E+00	2.2157E+00	2.2514E+00	2.3079E+00	2.3459E+00	2.4057E+00	2.4441E+00	2.5059E+00	2.5481E+00	2.6078E+00	2.6529E+00	2.7125E+00
18	5.3109E-06	1.4380E-04	1.5601E-03	8.6905E-03	2.5994E-02	3.8190E-02	1.8013E-02	4.7792E-04	2.3667E-02	1.2690E-02	5.2854E-03	2.4249E-02	1.3981E-05	2.5433E-02	8.2980E-04	2.5639E-02	6.7558E-04	2.7862E-02	1.5369E-04	2.7694E-02
	1.7277E+00	1.7847E+00	1.8384E+00	1.8901E+00	1.9405E+00	1.9903E+00	2.0400E+00	2.0837E+00	2.1383E+00	2.1914E+00	2.2279E+00	2.2861E+00	2.1299E+00	2.3832E+00	2.4585E+00	2.4825E+00	2.5585E+00	2.5836E+00	2.5875E+00	2.6854E+00
19	2.7736E-06	8.0404E-05	9.4212E-04	5.7548E-03	1.9401E-02	3.4100E-02	2.3626E-02	5.9922E-04	1.4983E-02	1.9560E-02	1.2830E-04	2.1958E-02	4.3608E-03	1.5415E-02	1.0444E-02	1.1984E-02	1.2273E-02	1.3697E-02	9.1538E-03	2.0573E-02
	1.7088E+00	1.7670E+00	1.8215E+00	1.8735E+00	1.9241E+00	1.9738E+00	2.0233E+00	2.0757E+00	2.1210E+00	2.1725E+00	2.1633E+00	2.2666E+00	2.3265E+00	2.3621E+00	2.4201E+00	2.4600E+00	2.5185E+00	2.5607E+00	2.6191E+00	2.6625E+00

Table C.3: CN Red: Franck-Condon factor, r-centroid (Bohr)

v'\v"	0	1	2	3	4	5	6	7	8	9
0	4.9295E-01	3.7338E-01	1.1391E-01	1.8078E-02	1.5994E-03	7.7632E-05	1.8498E-06	1.5133E-08	9.3691E-13	5.1899E-13
	2.2793E+00	2.3677E+00	2.4664E+00	2.5784E+00	2.7097E+00	2.8727E+00	3.1003E+00	3.5268E+00	1.1853E+01	3.1500E+00
1	3.2173E-01	4.1989E-02	3.4735E-01	2.2599E-01	5.5812E-02	6.7074E-03	4.0836E-04	1.1472E-05	1.0224E-07	2.8454E-12
	2.2020E+00	2.3125E+00	2.3838E+00	2.4807E+00	2.5925E+00	2.7242E+00	2.8890E+00	3.1219E+00	3.5734E+00	1.6794E+01
2	1.2841E-01	2.3688E-01	1.3934E-02	2.0626E-01	2.8977E-01	1.0664E-01	1.6810E-02	1.2500E-03	4.0559E-05	3.8597E-07
	2.1328E+00	2.2183E+00	2.2511E+00	2.4028E+00	2.4958E+00	2.6069E+00	2.7391E+00	2.9056E+00	3.1439E+00	3.6225E+00
3	4.1056E-02	1.9567E-01	9.4579E-02	9.2884E-02	8.0661E-02	2.9817E-01	1.6132E-01	3.2640E-02	2.9086E-03	1.0721E-04
	2.0704E+00	2.1469E+00	2.2394E+00	2.2956E+00	2.4291E+00	2.5118E+00	2.6218E+00	2.7543E+00	2.9226E+00	3.1667E+00
4	1.1669E-02	9.6506E-02	1.8023E-01	1.3360E-02	1.5063E-01	1.3056E-02	2.6334E-01	2.1115E-01	5.4117E-02	5.6987E-03
	2.0136E+00	2.0837E+00	2.1622E+00	2.2860E+00	2.3158E+00	2.4917E+00	2.5291E+00	2.6372E+00	2.7699E+00	2.9400E+00
5	3.1103E-03	3.7311E-02	1.3487E-01	1.1924E-01	2.8267E-03	1.5685E-01	1.3689E-03	2.0394E-01	2.4966E-01	8.0459E-02
	1.9618E+00	2.0265E+00	2.0975E+00	2.1795E+00	2.1345E+00	2.3342E+00	2.1766E+00	2.5485E+00	2.6532E+00	2.7858E+00
6	8.0241E-04	1.2621E-02	6.9308E-02	1.4140E-01	5.4634E-02	3.3575E-02	1.2389E-01	2.5860E-02	1.3784E-01	2.7314E-01
	1.9144E+00	1.9744E+00	2.0397E+00	2.1122E+00	2.2019E+00	2.2301E+00	2.3536E+00	2.3837E+00	2.5713E+00	2.6699E+00
7	2.0444E-04	3.9543E-03	2.9172E-02	9.6354E-02	1.1890E-01	1.2419E-02	7.2829E-02	7.5721E-02	6.4334E-02	7.8601E-02
	1.8710E+00	1.9268E+00	1.9873E+00	2.0535E+00	2.1280E+00	2.2443E+00	2.2564E+00	2.3765E+00	2.4206E+00	2.6006E+00
8	5.2150E-05	1.1871E-03	1.0927E-02	4.9999E-02	1.0953E-01	8.0434E-02	3.5035E-05	9.8861E-02	3.2791E-02	9.9458E-02
	1.8314E+00	1.8833E+00	1.9395E+00	2.0007E+00	2.0679E+00	2.1460E+00	1.1913E+00	2.2764E+00	2.4092E+00	2.4445E+00
9	1.3444E-05	3.4896E-04	3.8164E-03	2.2172E-02	7.0050E-02	1.0554E-01	4.1209E-02	1.1594E-02	1.0351E-01	6.6842E-03
	1.7950E+00	1.8434E+00	1.8958E+00	1.9526E+00	2.0144E+00	2.0831E+00	2.1685E+00	2.1643E+00	2.2953E+00	2.4863E+00

Table C.4: CN Violet: Franck-Condon factor, r-centroid (Bohr)

v'\v"	0	1	2	3	4	5	6	7	8	9
0	9.1934E-01	7.4850E-02	5.4294E-03	3.5468E-04	2.2258E-05	1.4482E-06	1.1102E-07	1.1603E-08	1.7366E-09	3.4370E-10
	2.2030E+00	1.9771E+00	1.8204E+00	1.6620E+00	1.5036E+00	1.3600E+00	1.2772E+00	1.3004E+00	1.3995E+00	1.4989E+00
1	7.9263E-02	7.7666E-01	1.2835E-01	1.4326E-02	1.2806E-03	1.0361E-04	8.3295E-06	7.5491E-07	8.8998E-08	1.4506E-08
	2.4383E+00	2.2208E+00	1.9840E+00	1.8313E+00	1.6765E+00	1.5234E+00	1.3836E+00	1.2959E+00	1.3044E+00	1.3905E+00
2	1.3948E-03	1.4495E-01	6.6065E-01	1.6470E-01	2.5109E-02	2.8727E-03	2.8708E-04	2.7699E-05	2.9102E-06	3.8062E-07
	2.8199E+00	2.4571E+00	2.2400E+00	1.9898E+00	1.8416E+00	1.6901E+00	1.5420E+00	1.4060E+00	1.3148E+00	1.3081E+00
3	4.1021E-08	3.5280E-03	1.9966E-01	5.6698E-01	1.8745E-01	3.6555E-02	5.1269E-03	6.1392E-04	6.9535E-05	8.3510E-06
	-1.0445E+01	2.8653E+00	2.4763E+00	2.2608E+00	1.9943E+00	1.8513E+00	1.7028E+00	1.5593E+00	1.4270E+00	1.3338E+00
4	4.5280E-07	2.0910E-06	5.8811E-03	2.4552E-01	4.9200E-01	1.9959E-01	4.7757E-02	7.9645E-03	1.1173E-03	1.4602E-04
	2.5934E+00	-8.7011E-01	2.9159E+00	2.4960E+00	2.2835E+00	1.9974E+00	1.8606E+00	1.7145E+00	1.5754E+00	1.4468E+00
5	9.4770E-10	2.1538E-06	1.4810E-05	8.0505E-03	2.8423E-01	4.3266E-01	2.0356E-01	5.8090E-02	1.1257E-02	1.8180E-03
	-6.4219E-02	2.6867E+00	6.6839E-01	2.9736E+00	2.5163E+00	2.3084E+00	1.9985E+00	1.8695E+00	1.7255E+00	1.5906E+00
6	1.6993E-10	1.3850E-08	5.9074E-06	5.6654E-05	9.7304E-03	3.1713E-01	3.8645E-01	2.0136E-01	6.7154E-02	1.4848E-02
	3.2302E+00	9.3512E-01	2.7870E+00	1.3124E+00	3.0407E+00	2.5371E+00	2.3356E+00	1.9975E+00	1.8782E+00	1.7357E+00
7	2.4625E-12	9.9119E-10	8.8420E-08	1.2054E-05	1.5720E-04	1.0704E-02	3.4523E-01	3.5133E-01	1.9456E-01	7.4741E-02
	1.9380E+00	3.5010E+00	1.4318E+00	2.8994E+00	1.6761E+00	3.1209E+00	2.5587E+00	2.3652E+00	1.9938E+00	1.8868E+00
8	1.1849E-13	4.7672E-11	2.6644E-09	3.6805E-07	1.9937E-05	3.5627E-04	1.0842E-02	3.6923E-01	3.2570E-01	1.8439E-01
	3.3487E+00	2.2771E+00	3.9589E+00	1.7437E+00	3.0328E+00	1.9168E+00	3.2203E+00	2.5809E+00	2.3971E+00	1.9865E+00
9	1.0733E-14	6.7681E-13	3.1011E-10	4.1715E-09	1.1655E-06	2.7567E-05	7.0052E-04	1.0107E-02	3.8953E-01	3.0832E-01
	2.4002E+00	3.7548E+00	2.4939E+00	4.8106E+00	1.9681E+00	3.2027E+00	2.0934E+00	3.3490E+00	2.6040E+00	2.4311E+00